Large-Eddy Simulation of smooth and rough channel flows using a one-dimensional stochastic wall model

Livia S. Freire^a, Marcelo Chamecki^b

^aUniversity of São Paulo, São Carlos, São Paulo, Brazil

^b University of California, Los Angeles, California, USA

6 Abstract

3

5

In this study a stochastic wall model based on the "large-eddy" version of the One-Dimensional Turbulence (ODT) model was developed for Large-Eddy Simulation (LES) of smooth and rough channel flows, with the primary goal of providing a refined turbulent flow field near the wall. This LES-ODT coupling was tested with the dynamic Smagorisky and the 10 scale-dependent Lagrangian dynamic subgrid-scale models. When compared to the same LES 11 with a wall model based on a local law-of-the-wall, LES-ODT improved the one-dimensional 12 energy spectra for all three velocity components close to the wall for both subgrid-scale 13 models tested. More importantly, improving the LES wall model had a more positive effect 14 in the near-wall spectra than improving the subgrid-scale model from the traditional dynamic 15 to the scale-dependent Lagrangian dynamic model. For smooth channels, LES-ODT results 16 compared well with DNS of $Re_{\lambda} = 590$ and 5200; however, the variance modeled by the 17 ODT presents discrepancies for all three velocity components, an issue inherent to ODT. Finally, the simulation of a channel flow with additional roughness modeled by a drag force 19 was compared to data of atmospheric flow through a maize field, providing evidence of the potential for this approach to directly simulate complex near-wall phenomena. Given its 21 high computational cost, the main use of the LES-ODT coupling is in studies that require a refinement of the near-wall region without the need to refine the entire LES domain. 23

- 24 Keywords:
- Large-eddy simulation, one-dimensional turbulence, rough channel flow, smooth channel
- 26 flow, wall model

27 1. Introduction

The study of high-Reynolds-number wall-bounded flows, such as boundary layers and channels, provides a cornerstone for many applied engineering and environmental problems, including flows in ducts, rivers, and the boundary layer of the atmosphere and ocean. The Direct Numerical Simulation (DNS) of such flows is limited by computational cost, and to our knowledge the channel-flow simulation with the highest Reynolds number so far was performed by Yamamoto and Tsuji [1], providing results for Re_{τ} up to 8000 ($Re_{\tau} = u_*\delta/\nu$ is the friction Reynolds number, where u_* is the friction velocity, δ is half-channel height and ν is kinematic viscosity). For applications in which higher Reynolds numbers are needed, Large-Eddy Simulation (LES) became the main numerical tool. In LES of wall-bounded flows, at least two options are available to treat the wall: (i) to adopt a vertically stretched grid so

that the first grid points are within the viscous sublayer and a no-slip boundary condition can be enforced at the wall (also known as wall-resolving LES or WRLES) [2, 3, 4, 5]; or 39 (ii) to have the wall-adjacent LES grid point above the viscous sublayer, which requires the 40 use a wall model to provide the missing information to the outer flow field (also known as 41 wall-modelled LES or WMLES) [6, 7, 8]. The issue with option (i) is that its computational cost can also be too high, since with the increase of the bulk Reynolds number (Re) the 43 turbulence scales of the inner layer decreases much faster than the scales of the outer layer, generating a computational cost that scales with $Re^{2.4}$ (due to the inner layer, compared to $Re^{0.6}$ for the outer layer alone) and limiting this option to moderate Reynolds numbers [9]. Option (ii), on the other hand, is not restricted by Reynolds number [10] and can be applied 47 to the problem of rough surfaces, parameterized in the wall model. Option (ii) can be further categorized into two groups: (ii-a) the RANS/LES hybrid formulation, in which the near-49 wall layer is resolved by RANS (Reynolds-Averaged Navier-Stokes) equations, and (ii-b) the wall-stress modeling approach, in which special boundary conditions are deployed to account 51 for the effects of the unresolved near-wall flow [11, 12]. In the (ii-b) category, the most simple 52 model relies on the assumption that within the LES time step a constant-stress layer exists 53 near the wall, implying that some variation of the logarithmic profile can be applied to the velocity field resolved by the LES (log-law wall model). This approach provides satisfying 55 results especially in environmental and geophysical applications, where Reynolds number is 56 extremely high and geometry is typically simple [9]. A more sophisticated approach in (ii-b), 57 known as two-layer model, is obtained by solving the thin, two-dimensional boundary-layer 58 equation, in which the time evolution of the wall-parallel velocity field is solved in a wallnormal refined grid within the first LES grid, providing the shear stress at the wall at each 60 LES time-step (wall-normal velocity is obtained by imposing continuity). In this thin layer, the flow behaves like a Stokes flow driven by the LES, and an eddy viscosity model represents 62 all the near-wall turbulent scales [13, 12]. Therefore, as in the RANS/LES approach, the wall layer is treated in a Reynolds-averaged sense [14]. 64

One of the main challenges of simulating wall-bounded flows with wall-modeled LES is the correct representation of turbulence structures close to the wall. As they get smaller due to wall blockage, a larger fraction of the turbulence needs to be correctly captured by the SGS model. The constant-coefficient Smagorinsky SGS model, for example, provides satisfactory results in the simulation of isotropic turbulence, but it is overdissipative close to the wall. This effect has direct consequences in the variance of the velocity components, and can be easily observed in the energy spectra [8]. The dynamic model, which uses the resolved scales of the flow to adjust the Smagorinsky coefficient, is in turn underdissipative close to the wall [8]. A more sophisticated version of these models, known as scale-dependent Lagrangian dynamic SGS model, takes into account the scale-dependence of the Smagorinsky coefficient, in addition to performing averages in time along lagrangian paths instead of relying on homogeneous directions of the flow. As evaluated by Bou-Zeid et al. [8], for Smagorinsky-type SGS models with a log-law wall model, this approach provides the best results close to the wall, with clear k^{-1} and $k^{-5/3}$ scaling ranges (k is wavenumber) in the streamwise velocity spectra.

65

68

70

71

72

73

74

77

79

81

Despite the overall satisfactory results provided by the combination of a log-law wall model and the scale-dependent Lagrangian dynamic SGS model, when near-wall turbulence is the main focus of the problem, there is still concern regarding the accuracy of the re-

sults. Because most wall models either explicitly or implicitly treat the near-wall region in a Reynolds-averaged sense, near-wall dynamics might not be acceptable for some applications, 84 such as the transport of matter very close to the wall. Motivated by this issue, Schmidt et al. [14] proposed a stochastic wall model that simulates the instantaneous velocity field without 86 averaging assumptions, which can also be seen as a wall-stress model in a two-layer approach as the thin boundary layer model [15], but in this case near-wall velocity fluctuations are 88 also present. In this approach, the One-Dimensional Turbulence (ODT) model proposed by Kerstein et al. [16] is used as a column model embedded within each wall-adjacent LES grid 90 to refine the flow field information in the vertical direction, providing turbulence information 91 in scales smaller than the ones resolved by the LES. The ODT is instantaneously forced by 92 the LES, which in turn uses ODT information as a lower boundary condition. This two-93 way coupling provided satisfactory results when compared to smooth-channel DNS results 94 of $Re_{\tau} = 395$ and 590, and presented the correct trend with Re_{τ} for mean flow and velocity 95 variances for Re_{τ} up to 10000. In addition to providing an improved instantaneous boundary 96 condition, this approach has the advantage of providing refined wall-normal turbulent flow 97 field that can incorporate a diverse set of phenomena, such as buoyancy, chemical reactions, 98 drag force and source/sink profiles, in a straightforward manner similar to what is typically gg done in LES [16, 17, 18]. Therefore, this approach represents not only a potential improve-100 ment in LES near-wall turbulence, but also an alternative to simulate complex phenomena 101 very close to the wall that are directly impacted turbulence. However, because in this case 102 the ODT resolved the viscous layer, the computational cost of the overall simulation scaled 103 with $Re_{\tau}^{2.3}$, which is similar to WRLES. 104

In this study, we develop a new wall model based on the "large-eddy" version of ODT developed by Freire and Chamecki [18], which is applicable to both rough and smooth channel flows. For rough channels, this formulation corresponds to a WMLES version whose computational cost is independent of Re_{τ} . The coupling between ODT and LES follows the original framework proposed by Schmidt et al. [14], and it is used to investigate the effects of ODT wall model on turbulence structure using different SGS models. We use an LES code that is typically employed in geophysical studies using the log-law wall model [19, 20, 21, 22], and comparisons with LES + log-law results are provided throughout the study. Although this LES-ODT approach is closer to two-layer models such as the thin boundary layer model, the comparison with the most simple wall-stress approach provides an opportunity to indentify the turbulence features that are already present in the LES with a simpler wall model, in contrast to the new features provided by ODT.

105

106

107

108

109

110

111

112

113

114

115

116

117

118

119

120

122

123

124

Motivated by environmental applications, we also develop an approach in which surface roughness is modeled via vertically resolved drag force within the ODT, and compare results to data measured in a maize field. When canopy is present, as in many other environmental problems (sediment transport, snow drift and deposition, breaking wave, etc), the relevant phenomena are too close to the surface to be captured by typical LES grid resolution when the entire boundary layer is simulated. In these cases, the usual approach is to restric the domain to a fraction of the region of interest [23, 24], reducing the scope of the study. Thus, in this context, the LES-ODT tool can also be used as an alternative in the investigation of near-wall dynamics in a large domain.

2. Models

2.1. The One-Dimensional Turbulence model

The aspects of the ODT model needed to understand its overall behavior and to reproduce the code will be presented here, but given its complexity and great amount of details, the reader is referred to more complete descriptions already present in the literature [14, 16, 25].

The one-dimensional stochastic model used in this study was developed by Kerstein [25] and successfully used as a stand-alone model to simulate different types of turbulent flows, including homogeneous turbulence, shear layers, buoyancy-driven flows [25], mixing-layer and wakes [16], jet diffusion flames [17], the stable atmospheric boundary layer [26], particle dispersion in homogeneous flows [27], passive scalar transport in channel flows [28] and flow through plant canopies [18]. The model corresponds to one-dimensional diffusion equations for all variables of interest (which in this study are the three velocity components, but temperature, scalar and particle concentration can be included in the same way), i.e.,

$$\frac{\partial u_i}{\partial t} = \nu \frac{\partial^2 u_i}{\partial z^2} + F_i + stochastic \ eddies \tag{1}$$

where u_i is the velocity vector (index notation is used when necessary), t is time, z is the vertical direction, F_i is the constant mean pressure gradient force that drives the flow and stochastic eddies correspond to the effect of three-dimensional turbulence in this one-dimensional field. The simulation is performed by evolving the diffusion equation in time, and at each time step a stochastic eddy can be selected from a probability distribution of eddy size and location in the domain. When a stochastic eddy is selected, all variables at the position z within the eddy are replaced by the value of the same variable at the position M(z), a mapping function that is a model for advection, mixing the variables and creating small-scale fluctuations in such a way that mimics the energy cascade of turbulent flows. It is conservative (i.e., it preserves the total amount of the quantity being transported) and it does not introduce discontinuities. Mathematically, it is defined as

$$M(z) = z_b + \begin{cases} 3(z - z_b), & \text{if } z_b \le z \le (z_b + l/3), \\ 2l - 3(z - z_b), & \text{if } (z_b + l/3) \le z \le (z_b + 2l/3), \\ 3(z - z_b) - 2l, & \text{if } (z_b + 2l/3) \le z \le (z_b + l), \\ z - z_b, & \text{otherwise,} \end{cases}$$

$$(2)$$

where l and z_b are the variables representing the size and bottom position of the eddy, respectively. As described by Kerstein and Wunsch [26], the mapping function "takes a line segment, shrinks it to a third of its original length, and then places three copies on the original domain; the middle copy is reversed, which maintains continuity of advected fields and introduces the rotational folding effect of turbulent eddy motion".

In addition to this mixing effect, when a *stochastic eddy* is selected, a second term creates redistribution of energy among velocity components, mimicking a pressure-induced tendency towards isotropy on the flow. The final model for the occurrence of *stochastic eddies* is

$$u_i(z) \to u_i(M(z)) + c_i[z - M(z)], \tag{3}$$

where c_i is the amplitude of the energy redistribution. For details in the assumptions used for its calculation, see Kerstein et al. [16] and Freire and Chamecki [18]. The final equation for c_i is

$$c_i = \frac{27}{4l} \left[-u_{K,i} \pm \sqrt{\frac{1}{3} \left(u_{K,1}^2 + u_{K,2}^2 + u_{K,3}^2 \right)} \right], \tag{4}$$

where the quantity inside the square root represents the total amount of energy inside the eddy available for redistribution, calculated using

$$u_{K,i} \equiv \frac{1}{l^2} \int_{z_b}^{z_b+l} u_i(M(z))[z - M(z)] dz.$$
 (5)

The final piece of information needed for the ODT is the probability distribution of eddy size and location, $\lambda(l, z_b; t)$, which also evolves in time with the flow. It is calculated from the instantaneous amount of kinetic and potential energy in the flow, adding another physical aspect to the stochastic model. The details of its derivation is also described in Kerstein et al. [16] and Freire and Chamecki [18], and its final formulation is given by

$$\lambda(z_b, l; t) = \frac{C_\lambda}{l^3} \sqrt{\frac{1}{3} \left(u_{K,1}^2 + u_{K,2}^2 + u_{K,3}^2 \right) - \frac{Z_\lambda \nu^2}{l^2}}.$$
 (6)

A proportionality constant C_{λ} is used to regulate the number of eddies for a given amount of energy, effectively setting the turbulence intensity. Another constant, Z_{λ} , adjusts the damping effect of viscosity, because any eddy with a time scale longer than the viscous time scale should be prohibited. The values of C_{λ} and Z_{λ} are the only tunable parameters, which can be different for different types of flows, but they are not expected to vary with Re_{τ} [14, 18].

Because ODT is based on the diffusion equation plus eddies with a size proportional to the grid size, it allows for a large-eddy approach similar to the LES, which was developed and tested by Kerstein and Wunsch [26] and Freire and Chamecki [18]. In this "large-eddy mode", ODT is "wall-modeled" and does not resolve the small scales of the flow, but a resolved velocity field is simulated instead. This is done by applying a filter with scale $\Delta_{\rm ODT}$ to Eq. (1), where $\Delta_{\rm ODT}$ is the fixed ODT grid size, separating resolved from subgrid scales and becoming

$$\frac{\partial \widetilde{u}_i}{\partial t} = \frac{\partial \tau_i}{\partial z} + F_i + stochastic \ eddies, \tag{7}$$

where \tilde{u}_i is the resolved velocity field and τ_i is the SGS vertical stress vector. The latter is modeled following Freire and Chamecki [18], which used a one-dimensional analogy to the eddy-viscosity model

$$\tau_i = -\nu_{SGS} \frac{\partial \widetilde{u}_i}{\partial z},\tag{8}$$

where the SGS eddy viscosity ν_{SGS} is given by

$$\nu_{SGS} = (C_s \, 6\Delta_{\text{ODT}})^2 \left[\frac{\partial \widetilde{u}_i}{\partial z} \frac{\widetilde{u}_i}{\partial z} \right]^{1/2}, \tag{9}$$

which uses the fact that the size of the smallest stochastic eddy is $6\Delta_{\rm ODT}$. The Smagorinsky coefficient C_s is calculated with a wall-damping function as

$$\frac{1}{(C_s 6\Delta_{\text{ODT}})^n} = \frac{1}{(C_{s,0} 6\Delta_{\text{ODT}})^n} + \frac{1}{[\kappa(z+z_0)]^n},$$
(10)

in which the parameters $C_{s,0} = 0.1$ and n = 2 were used [8, 21]. In the lowest ODT grid point, 187 vertical derivatives of horizontal velocity components are obtained from the law-of-the-wall 188 for a rough flow, namely

$$\frac{\partial \widetilde{u}_i}{\partial z} = \frac{u_*}{\kappa \Delta_{\text{ODT}}} \frac{\widetilde{u}_i}{(\widetilde{u}_1^2 + \widetilde{u}_2^2)^{1/2}}, \text{ with } u_* = \frac{\kappa}{\ln(\Delta_{\text{ODT}}/z_0)} (\widetilde{u}_1^2 + \widetilde{u}_2^2)^{1/2}$$
(11)

for i = 1, 2 and $\partial \widetilde{u}_3/\partial z = \widetilde{u}_3/\Delta_{\rm ODT}$. We note that, although the Smagorinsky model is not ideal for near-wall turbulence due to its overdissipative characteristic [8], the use of a dynamic estimation of C_s did not provide any improvement. Since the results obtained here are shown to be mesh-convergent, we chose to maintain the constant Smagorinsky approach for simplicity.

191

192

193

194

195

196

197

198

200

202

203

204

205

206

207

209

As discussed by Kerstein and Wunsch [26] and Freire and Chamecki [18], this "large-eddy mode" has the advantage of reducing computational cost, in addition to better representing rough surfaces that require a bulk parameterization (as a function of a "equivalent roughness height" parameter). Furthermore, in this approach the molecular viscosity term is removed as it is negligible compared to the other terms of the equation, and the viscous damping effect in the probability of stochastic eddies equation becomes irrelevant (the constant Z_{λ} is effectively set to zero). Therefore, this formulation does not have any viscous effect and it independent of Re_{τ} , representing very-high Reynolds number cases.

Finally, the roughness representation through a drag force is implemented by following the usual approach in LES, in which a drag force proportional to the square of the local velocity is used. Because we will compare this simulation with measurements of a flow through a maize field, the drag force here is defined as [24]

$$d_i = -C_d a(z) P_{ij} \widetilde{u}_j (\widetilde{u}_k \widetilde{u}_k)^{1/2}, \tag{12}$$

where C_d is the drag coefficient, a(z) is the leaf area density and P_{ij} is the projection matrix. This drag force parameterization is added to the RHS of Eq. (7). In addition, the energy 208 redistribution term (Eq. (4)) needs to include the energy lost to drag, and it is rewritten as [18]210

$$c_{i} = \frac{27}{4l} \left[-u_{K,i} \pm \sqrt{\frac{1}{3} \left(u_{K,1}^{2} + u_{K,2}^{2} + u_{K,3}^{2} - \frac{64}{81} C_{d} P \int_{z_{b}}^{z_{b}+l} a(z) e(z) dz \right)} \right], \quad (13)$$

where $P = P_{ii}/3$ and $e = (\tilde{u}_1 + \tilde{u}_2 + \tilde{u}_3)/2$ is the resolved kinetic energy. Different from Freire and Chamecki [18], the energy lost to drag is applied in both eddy selection (by adding the 212 drag term into Eq. (6)) and energy redistribution. Note also that other forms of drag force could be used to model other types of roughness.

The ODT model is solved explicitly, using forward Euler method for the time discretization. The upper limit in $\Delta t_{\rm ODT}$ comes from the stochastic eddies implementation, as follows. In principle, at each time step the eddy rate distribution $\lambda(z_b,l;t)$ should be updated, and eddies should be selected from it. In practice, this would result in a high computational cost because of all possibilities of eddy position z_b and eddy size l. For that reason, what is actually implemented is a statistical approximation (called "rejection method"), in which at each time step a candidate eddy (that may or may not be implemented) is selected from two random distributions f(l) and $g(z_b)$ (constant in time), having $\lambda(z_b^*, l^*; t)$ estimated only for the selected pair (z_b^*, l^*) . These candidate eddies are then accepted it at a rate P, such that $P(z_b^*, l^*, t, \Delta t) = \lambda(z_b^*, l^*; t) \Delta t_{\rm ODT}/(f(l^*)g(z_b^*))$, by sampling random numbers between zero and one. In the limit of $\Delta t_{\rm ODT} \to 0$, this procedure is equivalent to sampling at rate $\lambda(z_b, l; t)$. This approximation generates similar results as long as $P \ll 1$ (the majority of the candidates are rejected), which is achieved by reducing $\Delta t_{\rm ODT}$. The choices of f(l) and $g(z_b)$ do not affect the final statistics, and $g(z_b)$ following a uniform distribution and $f(l) \sim l^{-2}$ were chosen, in addition to a maximum P of 0.05 [25].

2.2. Large-Eddy Simulation code

The LES code used in this study, also known as LESGO code [29], solves the filtered Navier-Stokes equation in a vertically staggered grid with fixed size. The numerical discretization combines a fully dealised pseudo-spectral method in the horizontal directions and a second-order centered finite-difference in the vertical direction. The fully explicit second-order Adams-Bashforth scheme is used for time integration. A constant mean pressure gradient force is imposed in the streamwise direction and horizontal boundary conditions are periodic, while a stress-free boundary condition is applied at the top of the domain. For the bottom boundary condition, the vertical velocity is defined at z=0 and is set to zero. The horizontal velocities are defined at $z=\Delta z/2$, which should be located in the logarithmic sublayer of the flow. Their bottom boundary condition is obtained from the local law-of-the-wall formulation (Neumann boundary condition) using a horizontal spatial filtering in the scale 2Δ to compensate for the log-law mismatch of the mean velocity gradient [29]. Two SGS models are tested here: (i) the standard scale invariant dynamic model with planar averaging (PASI) [30] and (ii) the Lagrangian-averaged scale-dependent dynamic model (LASD) [8]. More details of the code can be found in Bou-Zeid et al. [8].

In order to couple the LES code with ODT, it is necessary to adjust the representation of the advection term of the Navier-Stokes equation, which was originally written in the rotational form, i.e.,

$$\frac{\partial \widetilde{U}_i}{\partial t} + \widetilde{U}_j \left(\frac{\partial \widetilde{U}_i}{\partial x_j} - \frac{\partial \widetilde{U}_j}{\partial x_i} \right) = -\frac{1}{\rho} \frac{\partial p}{\partial x_i} + \tau_{ij}^{\text{LES}} + \widetilde{F}_i, \tag{14}$$

where \widetilde{U}_i is the LES resolved velocity field, p is a modified pressure term and τ_{ij}^{LES} is the SGS stress tensor [8]. Here we write the second term in the LHS of Eq. (14) in the divergence form, i.e. $\partial(\widetilde{U}_i\widetilde{U}_j)/\partial x_j$, which does not impact the statistics of the simulation (including mean, variances and spectra, not shown), as already observed for a fully dealised spectral code [31].

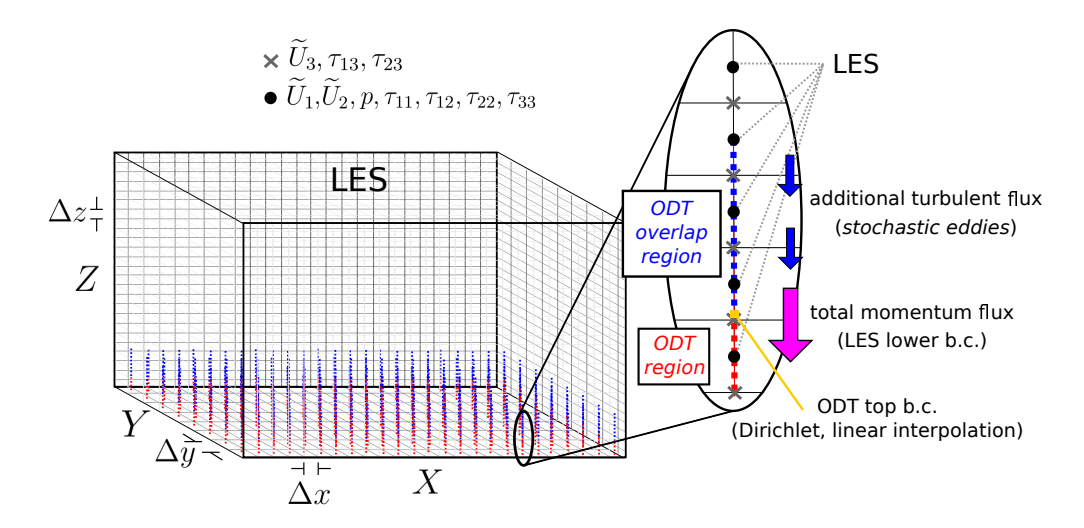


Figure 1: Illustration of the LES-ODT coupling. The ODT model is solved in the *ODT region*, which corresponds to the LES grids adjacent to the wall (domain size Δz). The *ODT overlap region* corresponds to the linear interpolation of the LES velocity field up to $z=3.5\Delta z$, where stochastic eddies are allowed to extend. The coupling has four elements: (i) the ODT is forced by LES through a top boundary condition (at $z=\Delta z+\Delta_{\rm ODT}$, from the linear interpolation between ODT and LES velocity fields), (ii) the LES velocity field in the wall-adjacent grid points is replaced by the ODT values, (iii) the total momentum flux from ODT within the lowest LES grids is used as a LES bottom boundary condition (additional ODT turbulent momentum flux within the second and third LES grids also goes into LES) and (iv) there is a horizontal advection among ODT columns driven by the LES velocity field. The vertically staggered grid configuration for the velocity components, pressure and shear stress is indicated by the black dots and grey crossings, where directions 1 (x), 2 (y) and 3 (z) correspond to streamwise, spanwise and vertical direction, respectivelly.

2.3. LES-ODT coupling

When used as a wall model, ODT corresponds to vertical lines embedded within each wall-adjacent LES grid (Fig. 1). Overall, the two-way coupling between the models can be listed as four steps: (i) ODT is forced by LES through a top boundary condition, (ii) the LES velocity field in the lowest grid points is replaced by the ODT values, (iii) the shear stress in the ODT is used as a LES bottom boundary condition and (iv) there is advection among ODT columns driven by the LES velocity field. The details of these four steps are described next.

The LES domain corresponds to a box with size $X \times Y \times Z$ (streamwise, spanwise and vertical directions, respectively) with $N_x \times N_y \times N_z$ grid points and grid sizes $\Delta x \times \Delta y \times \Delta z$. Each ODT domain corresponds to the height of the lowest grid, i.e., $Z_{\text{ODT}} = \Delta z$, and $\Delta_{\text{ODT}} = \Delta z/N_{\text{ODT}}$, where N_{ODT} is the number of grid points in each ODT model. This first (from bottom to top) LES grid that corresponds to the ODT domain will be called *ODT region*. There is no specific restriction on the size of Δz related to the LES-ODT coupling. There is, however, a minimum number of ODT grid points N_{ODT} in order to garantee an appropriate amount of "resolved turbulence" in the ODT (through the stochastic eddies), as it will be explored in the Results section.

A second ODT domain, called *ODT overlap region*, corresponds to $\Delta z \leq z \leq 3.5\Delta z$ (from the top of the first LES grid to the middle of the fourth LES grid, from bottom to top, Fig. 1), with the same grid size $\Delta_{\rm ODT}$. In this region, ODT is not advanced in time, but it has a velocity field calculated as a linear interpolation between the ODT and the LES

values within the region, which is used to allow stochastic eddies to extend beyond Δz . This means that stochastic eddies with bottom inside the ODT region $(z_b \leq \Delta z)$ but with size that goes beyond the ODT region are allowed to exist. A consistency test for the size of the overlap region was performed by Schmidt et al. [14] and it is reproduced here (see Appendix A), showing that the size of $3.5\Delta z$ provides the appropriate transition between the size of the largest stochastic eddies and the small resolved scales in the LES, as evidentiated by its effect in the mean velocity gradient.

In the LES-ODT coupling, three velocity fields are defined: (i) \widetilde{U}_i is the LES resolved velocity field, (ii) \widetilde{u}_i is the ODT resolved velocity field, and (iii) \widetilde{v}_i is the ODT velocity field averaged over the LES time step, used to send the information from ODT to LES in the correct scale. For the two horizontal components, \widetilde{v}_i is calculated directly as the average over the LES time step Δt , as they have an advecting quality in them. The vertical component, on the other hand, is conceptualized as a "representation of the wall-normal velocity component kinetic energy per unit mass (actually the square root of that energy)" [14], since the vertical transport is performed by the *stochastic eddies*. For that reason, \widetilde{v}_3 is calculated as

$$\widetilde{v}_3(z) = -\int_0^z \left(\frac{\partial \widetilde{v}_1}{\partial x} + \frac{\partial \widetilde{v}_2}{\partial y}\right) dz \tag{15}$$

in order to preserve continuity in the wall-adjacent LES grids. The velocity \tilde{v}_i has two uses in the simulation. In the ODT code, it is used to couple all the ODT columns via horizontal advection, which is accomplished by adding an advection term to the RHS of Eq. (7), i.e.,

$$\frac{\partial \widetilde{u}_i}{\partial t} = \frac{\partial \tau_i}{\partial z} + F_i + stochastic \ eddies + d_i - \frac{\partial (\widetilde{v}_j \widetilde{u}_i)}{\partial x_i}, \tag{16}$$

which is the final model for ODT in the LES-ODT coupling. Note that the horizontal advection happens in LES scale due to the coarseness of the X and Y directions, therefore the appropriate advective time scale is the LES rather than the ODT time scale, making the velocity field \tilde{v}_i the correct one for this task. Although this advection connects each ODT in a "LES-scale" sense, locally the core of the turbulent transport remains the *stochastic eddies* (and therefore one-dimensional), providing a model for local vertical advection and small-scale turbulence without the need to refine the grid in the horizontal directions.

The second use of \tilde{v}_i corresponds to the velocity field sent to the LES lowest grid points, i.e.,

$$\widetilde{U}_{i=1,2}(z=\Delta z/2) = \frac{1}{\Delta z} \int_0^{\Delta z} \widetilde{v}_{i=1,2}(z) dz \tag{17}$$

$$\widetilde{U}_{i=3}(z=\Delta z) = \widetilde{v}_{i=3}(z=\Delta z), \tag{18}$$

which enforces continuity in the vertically staggered grid configuration. This velocity field corresponds to one of two ODT results that go to the LES. In this step, there is no double-counting effect as the LES velocity is directly replaced by the ODT velocity.

The second coupling element provided to the LES is the vertical momentum flux within the wall-adjacent LES grids, which comes entirely from the ODT (also no double counting effect). It includes the momentum flux from the stochastic eddies, viscous diffusion or subgrid scale diffusion and vertical advection. These fluxes are accumulated (summed) during the ODT time steps within one LES time step, and they enter the LES code through the SGS stress tensor $\tau_{i3}(z \leq \Delta z)$. Additionally, the ODT fluxes caused by stochastic eddies that reach the ODT overlap region are also summed to the SGS stress tensor within the second and third grids $(\tau_{i3}(\Delta z < z \leq 3.5\Delta z))$. In this step, some mismatch can be caused by an excess or lack of additional flux, which is fixed by adjusting the size of the overlap region (see Appendix A) and the value of the ODT parameter C_{λ} (see Results section) in order to obtain the correct mean velocity gradient in the logarithmic region.

The linear interpolation performed in the *ODT-overlap region* is used to define a Dirichlet boundary condition immediately above the top of the ODT domain (at $z = \Delta z + \Delta_{\text{ODT}}$), passing the velocity field information from LES to ODT and closing the two-way coupling between the models.

After the evolution of the velocity field in time, a pressure Poisson equation is solved to impose continuity in the LES velocity field. In order to rematch the pressure-adjusted \widetilde{U}_i with \widetilde{v}_i , a pressure correction is applied to the ODT velocities \widetilde{u}_i and \widetilde{v}_i , which is calculated as

$$\widetilde{v}_{i=1,2,\text{new}} = \widetilde{v}_{i=1,2,\text{old}} - 2z \frac{\widetilde{v}_{i=1,2,\text{old}}}{\Delta z} + 2z \frac{\widetilde{U}_{i=1,2}}{\Delta z}.$$
(19)

After implementing the pressure correction in the horizontal components of \tilde{v}_i , Eq. (15) is used to update \tilde{v}_3 . Finally, the same procedure is performed to adjust the two horizontal components of \tilde{u}_i . As discussed by Schmidt et al. [14], this correction is not needed for \tilde{u}_3 , as it behaves only as a kinetic-energy reservoir for the energy transfer among velocity components, and no pressure effects need to be included in its evolution.

The description above sets the way in which ODT provides the lower boundary conditions to the LES, and how the LES creates a top boundary condition to the ODT. The ODT model is solved explicitly using forward Euler method for the time discretization, a second-order finite difference for the vertical derivatives and a fully-dealised pseudo-spectral method for the horizontal advection term, in order to be consistent with the LES code. The value of $\Delta t_{\rm ODT}$ is set as $\Delta t/15$ initially (as it solves smaller scales compared to LES), and it is reduced by a factor of two if the mean value of P (for all ODT's) during one LES time step is greater than 0.05. The ODT lower boundary condition is $\tilde{u}_i = 0$ for the smooth-channel cases, and a wall model based on the law-of-the-wall for the rough-channel cases (Eq. 11), in which z_0 is the roughness length scale. The sequence of steps of the LES-ODT simulation are summarized in Alg. 1.

The final detail that is important to mention is the parallelization of the LES-ODT coupling. Because the LES code is spectral in both horizontal directions, it was originally parallelized in the vertical direction, which is solved by the finite-difference method. The ODT model, on the other hand, cannot be parallelized in the vertical, as it needs its entire vertical information in each time step in order to select the appropriate *stochastic eddy*. Therefore, the parallelization of the ODT calculation is done in the streamwise direction, where each processor evolves a set of ODT domains. However, at each ODT time step, the horizontal advection term needs to be calculated using the same spectral method as in

```
Algorithm 1: LES-ODT algorithm in one LES time step
```

```
Input: \widetilde{u}_i(x, y, z_{\text{ODT}}, t), \widetilde{v}_i(x, y, z_{\text{ODT}}, t), \widetilde{U}_i(x, y, z, t)
Output: \widetilde{u}_i(x, y, z_{\text{ODT}}, t + \Delta t), \widetilde{v}_i(x, y, z_{\text{ODT}}, t + \Delta t), \widetilde{U}_i(x, y, z, t + \Delta t)
begin
     \widetilde{u}_i in overlap region (and top B.C.) \leftarrow linear interpolation of \widetilde{U}_i;
     t^* = t;
     repeat
           one stochastic eddy candidate is selected for each ODT;
           the accepted stochastic eddies are implemented through the triplet-map;
           \widetilde{u}_i(t^*) are advanced to \widetilde{u}_i(t^* + \Delta t_{\text{ODT}}) using the vertical diffusion equation
           (\tilde{v}_i(x, y, z_{\text{ODT}}, t) \text{ are used for advection});
           t^* = t^* + \Delta t_{\text{ODT}};
     until t^* = t + \Delta t;
     if horizontal and \Delta t average of P > 0.05 then
           \Delta t_{\rm ODT} = \Delta t_{\rm ODT}/2
     end
     \widetilde{v}_{1,2}(x, y, z_{\text{ODT}}, t + \Delta t) = \text{average of } \widetilde{u}_i \text{ between } t \text{ and } t + \Delta t;
     \widetilde{v}_3(x, y, z_{\text{ODT}}, t + \Delta t) \longleftarrow \text{incompressibility of } \widetilde{v}_{1,2}(x, y, z, t + \Delta t) \text{ (through Eq. 15)};
     \tau_{i3}^{\text{LES}}(x, y, \Delta z, t) = \text{advective} + stochastic eddies + SGS fluxes from ODT region;
     	au_{i3}^{\mathrm{LES}}(x,y,z,t) = 	au_{i3}^{\mathrm{LES}}(x,y,z,t) + stochastic \ eddies \ \mathrm{fluxes} \ \mathrm{from} \ ODT \ overlap \ \mathrm{fluxes}
     region;
     \widetilde{U}_i(x,y,z,t) are advanced to \widetilde{U}_i(x,y,z,t+\Delta t) using the filtered Navier-Stokes
     equation;
     \widetilde{U}_{1,2}(x,y,\Delta z/2,t+\Delta t) are replaced by the integral of \widetilde{v}_{1,2}(x,y,z_{\text{ODT}},t+\Delta t) over
      \Delta z (Eq. 17);
     \widetilde{U}_3(x, y, \Delta z, t + \Delta t) are replaced by \widetilde{v}_3(x, y, \Delta z, t + \Delta t);
     \widetilde{U}_i(x,y,z,t+\Delta t) are updated using the LES pressure Poisson equation;
     \widetilde{u}_i(x, y, z_{\text{ODT}}, t + \Delta t) and \widetilde{v}_i(x, y, z_{\text{ODT}}, t + \Delta t) are updated using pressure
     correction;
```

end

the LES through Fast Fourier Transform (FFT) in order to keep it in accordance with the numerics of the LES. This spectral calculation requires the ODT velocity information to be exchanged between all processors at each ODT time step, when the horizontal advection terms are calculated and redistributed back between the processors. The FFT calculation is shared among the processors in the vertical direction, but the need to exchange all information adds a significant computational cost to the simulation. This issue is particular to the numerics of this LES code, and was not present in the original work of Schmidt et al. [14], which was finite-difference in all three directions and ran in serial. An alternative to reduce part of this computational cost is to approximate the calculation of the advection term (last term of Eq. (16)) by updating the ODT velocity \tilde{u}_i in the LES time scale instead of the ODT time scale, i.e., to calculate the advection term only once at each ODT run. This approach was compared to the complete formulation for all flows tested here, and the error obtained was negligible for all statistics. Therefore this approximation is incorporated as part of the LES-ODT formulation in this study.

3. Summary of simulations

In this study, we start by evaluating the same rough channel flow simulations of Bou-Zeid et al. [8], in order to investigate the behavior of ODT wall model with two different SGS models: the planar-averaged scale-invariant dynamic model (PASI) and the Lagrangian-averaged scale-dependent dynamic model (LASD). The behavior of these two SGS models is re-evaluated using the local law-of-the-wall formulation (log-law) as a wall model, as performed by Bou-Zeid et al. [8]. In here we compare solutions obtained with the standard log-law wall model with solutions obtained by replacing the log-law with the ODT wall model in "large-eddy mode". This analysis allows us to choose the SGS model and the ODT parameter C_{λ} for the remaining simulations. Simulation parameters are detailed in Tab. 1, which are the same for all four simulations: PASI + log-law, PASI + ODT, LASD + log-law and LASD + ODT. The best value of $C_{\lambda} = 15$ was obtained by trial-and-error. Two additional simulations of LASD + ODT were performed with $C_{\lambda} = 14$ and 16 to demonstrate the sensitivity of the model. Because these rough channel cases are "wall modeled" and "large-eddy mode" for both LES and ODT, they do not have a Reynolds number defined, and should be interpreted as "very-high Reynolds number" cases.

The second set of simulations corresponds to smooth channels with $Re_{\lambda} = 590$ and 5200. These simulations were performed with ODT in "DNS mode", in addition to the LASD SGS model and $C_{\lambda} = 15$, defined as the best cases from the rough-channel analysis, and they are compared to DNS results of Lee and Moser [32] and Moser et al. [33]. Similar cases were also performed in the original LES-ODT model by Schmidt et al. [14], therefore the differences due to the LES code can be evaluated in this case. Table 2 lists the parameters used in these simulations. Because the smooth case has the additional adjustable parameter Z_{λ} for viscous cutoff, simulations with $Z_{\lambda} = 100$, 120 and 140 for $Re_{\tau} = 590$ were performed to demonstrate the sensitivity of the model to this parameter.

The last case evaluated here corresponds to a rough channel with additional roughness modeled by a drag force. This simulation is compared to data measured within and above a maize field by Gleicher et al. [34] during a 7-hour period of approximately neutral atmospheric conditions (without significant static stability effects). In this case, the maize field is

Table 1: Simulation parameters for LES with ODT in the rough channel case ($\delta=1$ and $u_*=1$) and maize field case ($\delta=342\,\mathrm{m},\ u_*=1$ and $h=2.1\,\mathrm{m}$). For the rough channel case, the same simulations were performed for LES with log-law wall model and LASD SGS model, for the following grid points: $N_x\times N_y\times N_z=256^3,128^3,64^3$, in addition to a simulation of LES with PASI SGS model and 64^3 grid points. For the maize field case, a LES with log-law wall model was performed with the same parameters below and $z_0=0.2\,\mathrm{m}$.

	rough channel	maize field
domain size $(X \times Y \times Z)$	$2\pi\delta \times 2\pi\delta \times \delta$	$2\pi\delta \times 2\pi\delta \times \delta$
number of grid points $(N_x \times N_y \times N_z, N_{\text{ODT}})$	$64 \times 64 \times 64, 8$	$64 \times 64 \times 64, 32$
	$64 \times 64 \times 64, 16$	
	$64 \times 64 \times 64, 32$	
	$64 \times 64 \times 64, 64$	
	$64 \times 64 \times 64, 96$	
	$128 \times 128 \times 128, 32$	
mean pressure gradient force $(F_i = \langle (1/\rho)(d\overline{p}/dx), 0, 0 \rangle)$	$\langle u_*^2/\delta,0,0\rangle$	$\langle u_*^2/\delta,0,0\rangle$
roughness height (z_0)	$1 \times 10^{-4} \delta$	$3 \times 10^{-5} \delta$
simulation time step (Δt)	$0.0002 \delta/u_*$	$0.0002\delta/u_*$
number of simulation time steps (N_t)	100 000	100000
total simulation time (eddy turnover times = δ/u_*)	20	20
eddy rate distribution parameters $(C_{\lambda}, Z_{\lambda})$	14, 0	$15^*, 0$
	$15^*, 0$	
	16, 0	

^{*}best C_{λ} value.

Table 2: Simulation parameters for LES with ODT in the smooth channel cases, in which $\delta = 1$ and $u_* = 1$. Similar simulation of LES with log-law wall model were performed, with $z_0 = \nu/7.77u_\tau$.

	$Re_{\tau} = 590$	$Re_{\tau} = 5200$
domain size $(X \times Y \times Z)$	$2\pi\delta\times2\pi\delta\times\delta$	$2\pi\delta \times 2\pi\delta \times \delta$
number of grid points $(N_x \times N_y \times N_z, N_{\text{ODT}})$	$32 \times 32 \times 16,32$	$128 \times 128 \times 128, 32$
mean pressure gradient force $(F_i = \langle (1/\rho)(d\overline{p}/dx), 0, 0 \rangle)$	$\langle u_*^2/\delta,0,0\rangle$	$\langle u_*^2/\delta,0,0\rangle$
simulation time step (Δt)	$0.00025 \delta/u_*$	$0.000125 \delta/u_*$
number of simulation time steps (N_t)	100000	200000
total simulation time (eddy turnover times = δ/u_*)	25	25
eddy rate distribution parameters $(C_{\lambda}, Z_{\lambda})$	15,100	$15,120^*$
	$15,120^*$	
	15,140	

^{*}best Z_{λ} value.

391

392

393

394

395

simulated by the ODT in "large-eddy mode", and the first LES grid point is located at 3.8h ($h = 2.1 \,\mathrm{m}$ is the canopy height). This simulation is also compared to LES results obtained by Pan et al. [24], in which the canopy was directly modeled by the LES with the same drag-force formulation (canopy-resolving LES). See simulation parameters in Tab. 1.

In all cases tested here, the LES code is initialized with a logarithmic profile in the

streamwise direction and zero velocity in speanwise and vertical directions, plus a uniformily distributed random fluctuation between zero and one in the three velocity components. All results presented in next section correspond to the average of the last six eddy turnover times of the simulations. Note that in the LES-ODT results, we chose to omit the first LES grid 399 from the figures because it comes directly from the ODT, which represents the true velocity with small scales fluctuations (LES and ODT results are not equal because the LES value is 401 an integral of the entire ODT domain, not the value of the ODT at the LES grid point).

4. Results

397

402

403

404

405

406

407

408

409

410

411

412

413

414

415

416

417

418

419

420

421

422

423

424

425

426

427

428

429

430

431

432

433

434

435

436

437

In this section, we use the rough channel case to evaluate LES results using log-law and ODT wall models, for different SGS models. After establishing the superiority of the LES-ODT with the LASD SGS model, we show that this approach is also appropriate for smooth channel simulations without the need of specific adjustments, except for the ODT viscous parameter. Finally we use the simulations of the maize field to discuss the possibility of using the ODT to incorporate complex near-surface physics that cannot be directly resolved in the LES in a large domain setup. A discussion regarding the computational cost and potential trade-off when using LES-ODT is provided at the end of the section.

4.1. Rough channel

The first consequence of the use of ODT directly observed at the beginning of the simulation is the early onset of turbulence. With the log-law wall model, turbulence starts after several thousands time steps, when local instabilities form close to the wall and spread through the horizontal domain, and then gradually grow in the vertical direction. With ODT, small-scale turbulence-like fluctuations start at the very beginning of the simulation, anticipating the onset of turbulence in the simulation to the initial time steps. This is due to the stochastic nature of the ODT, i.e., it is a consequence of the random fluctuations also present in the lower boundary condition in addition to the initial condition. Figure 2 shows a snapshot of rough-channel simulations with log-law and ODT wall models, for the LASD case. In the LES-ODT coupling, there is an instantaneous match between the two velocity fields, creating an additional region closer to the wall where turbulent structures can be resolved.

Figure 3 presents the vertical profiles of mean velocity, variances and total stress for the simulation with PASI and LASD SGS models, with log-law and ODT wall models. For the PASI case, using ODT improves the mean streamwise profile, correcting the underestimation in the logarithmic region (Fig. 3a). For all other statistics evaluated, results with log-law and ODT are similar, except for the variance of spanwise and vertical velocities close to the wall, which reduces (significantly in the spanwise case) when ODT is used (Fig. 3c,d). The difference in the first two grid points for the SGS and resolved stresses (Fig. 3e.f) is due to the implementation of the ODT momentum flux, which enters the LES as a SGS stress, but corresponds to the total stress at these locations. Because of that, the resolved stress at $z = \Delta z$ should be assumed zero by construction, although numerically it is different from zero (see discussion in Appendix B).

Figure 4 shows the sensitivity of the results to the C_{λ} parameter of the ODT eddy probability distribution, for the LASD case. The choice of $C_{\lambda} = 15$ was obtained by trial-and-

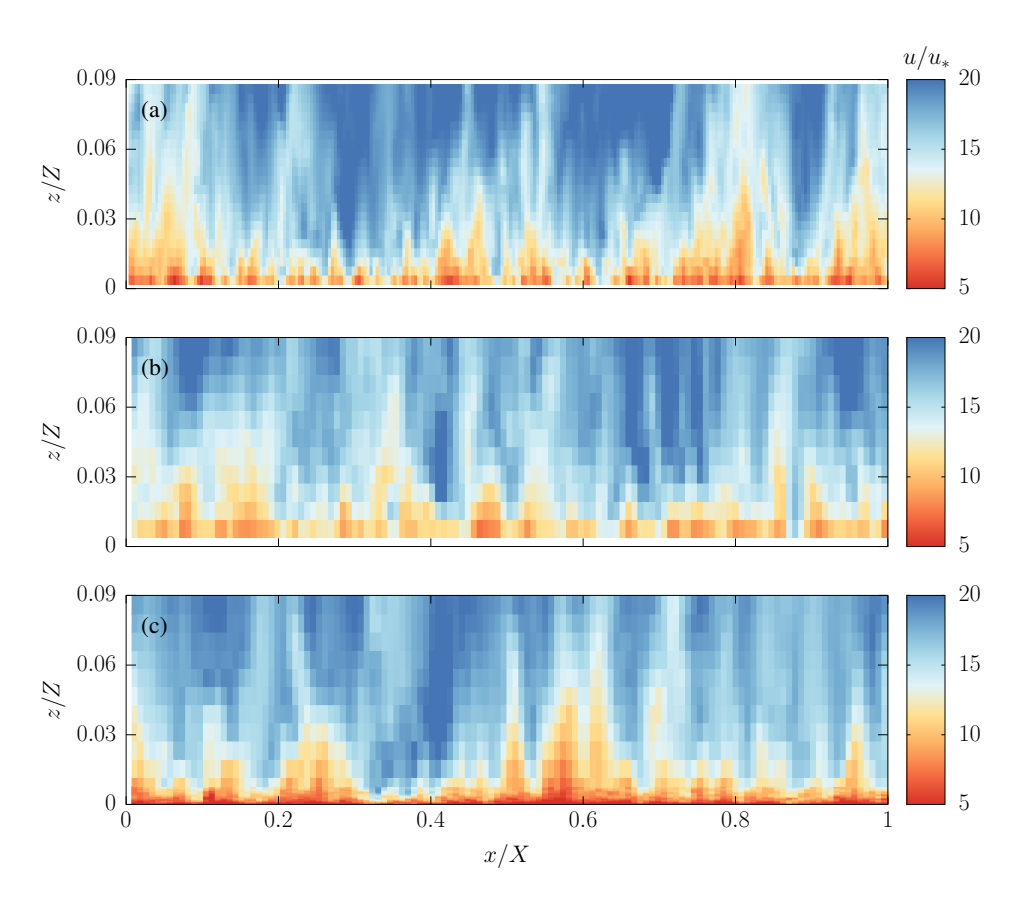


Figure 2: Snapshots of the streamwise velocity in the streamwise and vertical directions of rough channel case (LASD, $C_{\lambda}=15$): LES + log-law with (a) 256³ and (b) 128³ grid points, and (c) LES-ODT with $N=128^3$ and $N_{\rm ODT}=32$.

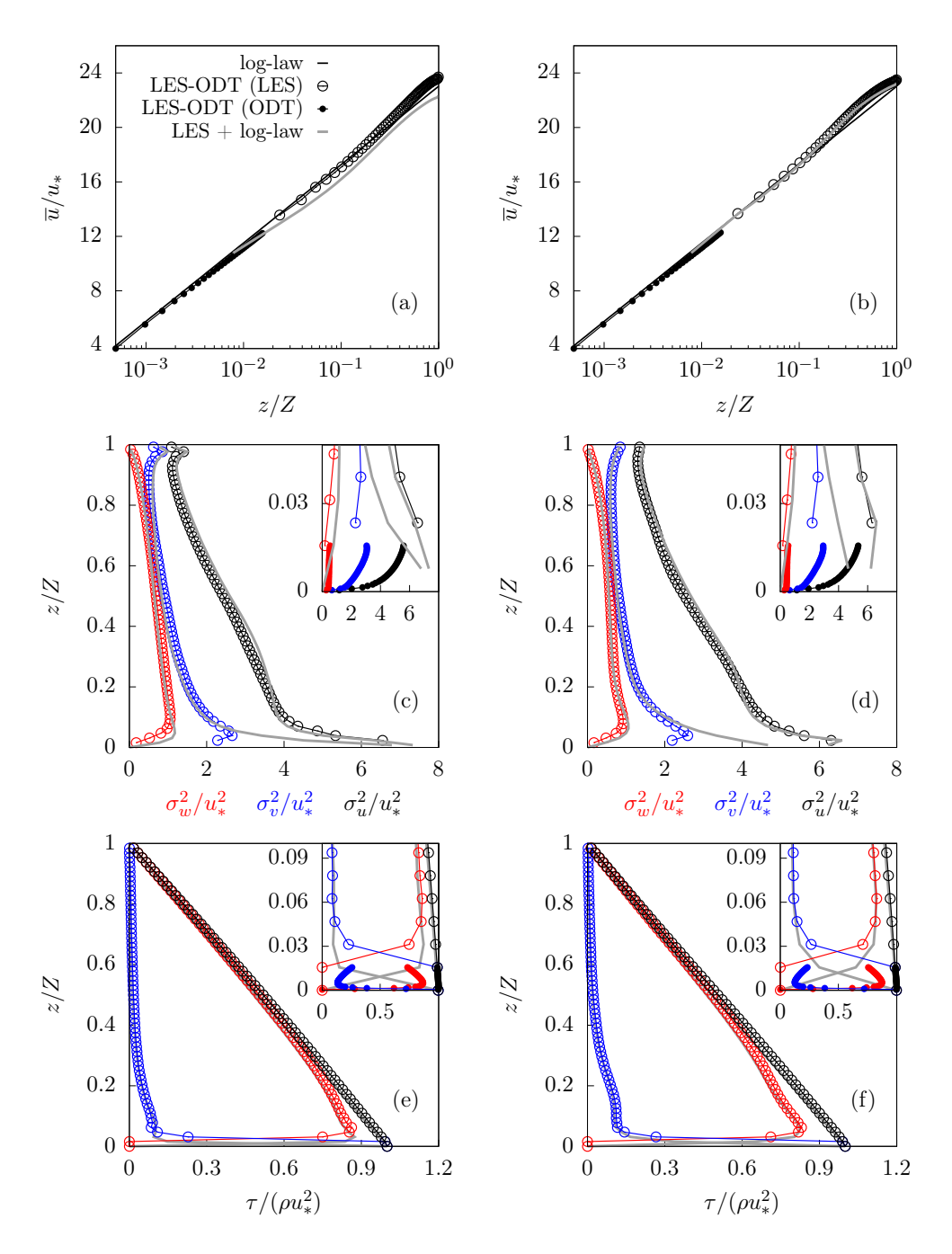


Figure 3: Results of LES-ODT (LES as open circles, ODT as filled circles) for the rough channel case and $N=64^3, N_{\rm ODT}=32$: (a, b) mean streamwise velocity, (c, d) variances of streamwise (black), spanwise (blue) and vertical (red) velocities, and (e, f) SGS (blue), resolved (red) and total (black) stress. Left column is PASI and right column is LASD SGS models. Gray lines correspond to LES + log-law and the same SGS models.

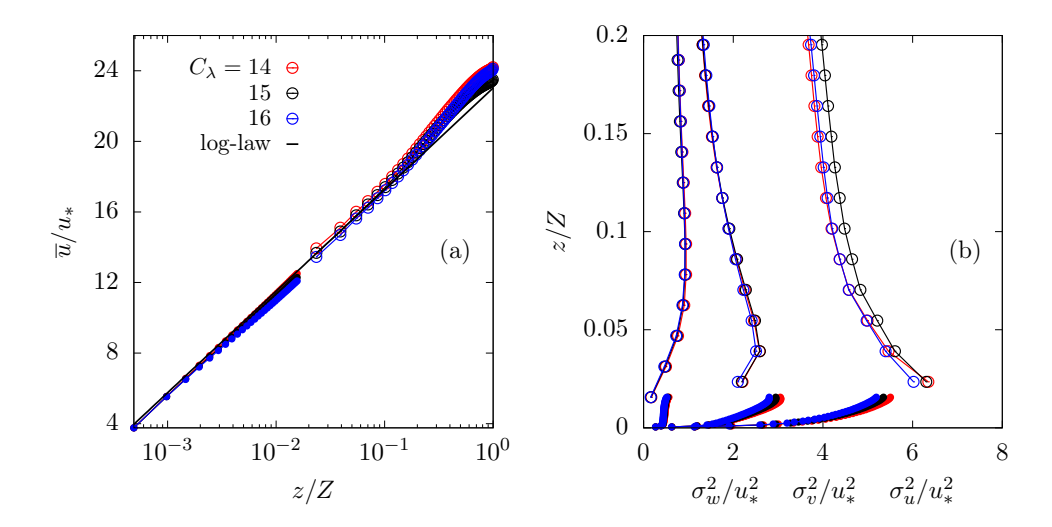


Figure 4: Sensitivity of LES-ODT simulation (LASD SGS model) to C_{λ} for the rough channel case (LES as open circles and ODT as filled circles): (a) mean streamwise velocity, (b) variances of streamwise (right), spanwise (middle) and vertical (left) velocities. Simulations with $C_{\lambda} = 14$ (red), 15 (black) and 16 (blue).

error, and its variation from 14 to 16 creates a small variation in the results. A reduction in C_{λ} causes a small overestimation of the velocity compared to the log-law, and a small increase in the horizontal variances, due to a reduction on the appropriate amount of *stochastic eddies*. The opposite trend is caused by an increase in C_{λ} .

438

439

440

441

442

443

444

445

446

447

448

449

450

451

452

453

454

455

456

457

458

459

460

461

462

463

The most clear evidence of the impact of ODT in the LES is in the energy spectra. Figures 5 and 6 compare the one-dimensional spectra of all three velocity components between log-law and ODT wall models, for PASI and LASD SGS models respectively. For the streamwise velocity, as discussed by Bou-Zeid et al. [8], PASI + log-law causes underdissipation close to the wall, resulting in a spectra with a slope flatter than the expected k^{-1} in the production range (Fig. 5a), which is significantly improved in the LASD + log-law case (Fig. 6a). For the spanwise and vertical velocities, however, both models yield spectra with underdissipation in the production range (Figs. 5c, e and 6c, e). The use of the ODT improves the production range behavior in all velocity components for both SGS models. The significant improvement in the spanwise velocity spectra (Figs. 5d and 6d) indicates that the reduction in spanwise velocity variance close to the wall (Fig. 3c,d) is likely an improvement caused by the ODT. The decrease in vertical velocity variance is also clear in the spectra closer to the wall. If we take the standard combination PASI + log-law as the reference case, improving the wall model alone (i.e., PASI + ODT) yields better near-wall spectra than improving the SGS model alone (i.e., LASD + log-law). As expected, the combination LASD + ODT produces the best results.

Although the LES + log-law results for spanwise variance has been published before (for example by Bou-Zeid et al. [8] and Stevens et al. [35] for this same code), its overestimation has not yet been discussed, to the best of our knowledge. One possible cause for this overestimation is the type of boundary condition used, as indicated by the study of Bae et al. [36]. In their wall-modeled channel flow simulation, the Neumann boundary condition provided the highest value for streamwise and spanwise variances in the first above-wall grid, compared to no-slip and slip boundary conditions. Although not exactly equal to the one

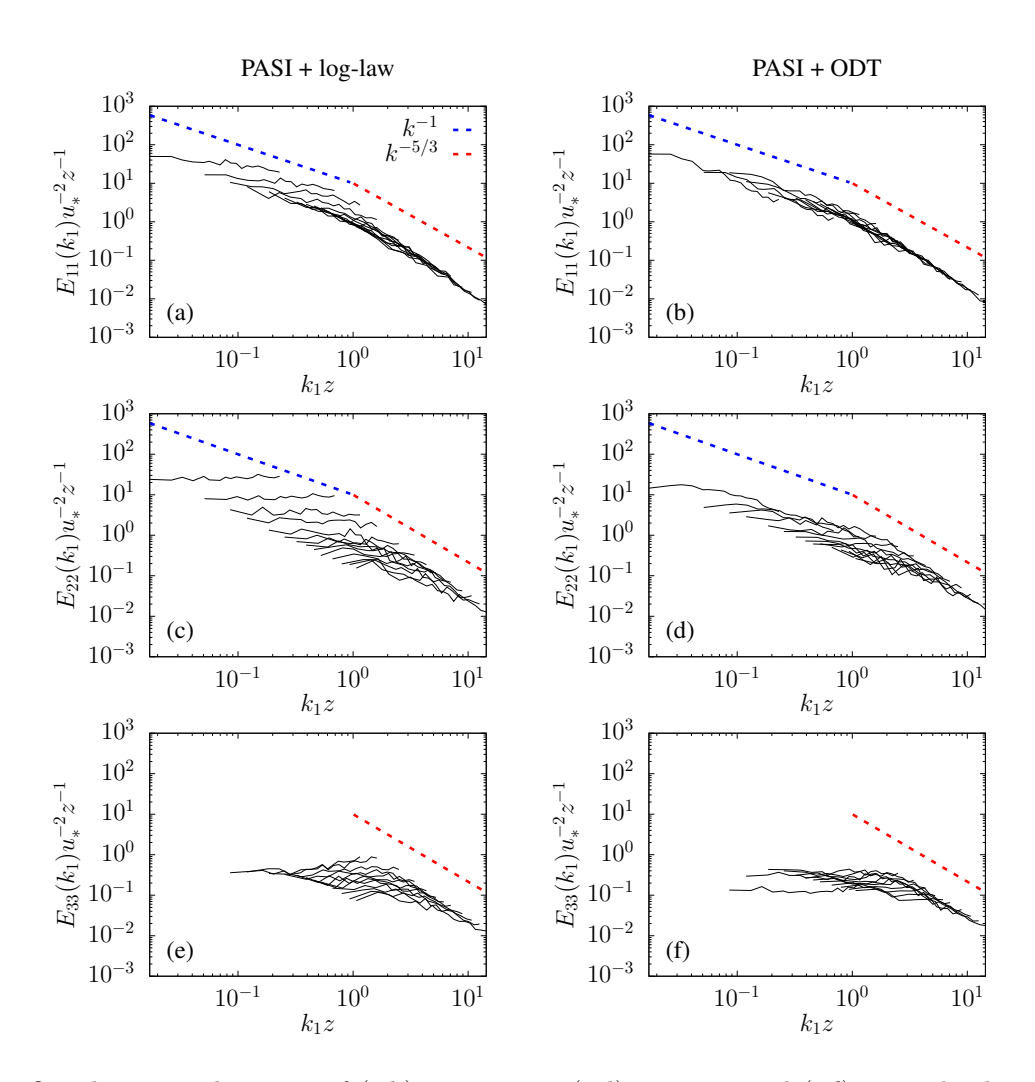


Figure 5: One-dimensional spectra of (a,b) streamwise, (c,d) spanwise and (e,f) vertical velocity, for z/Z from 0.008 to 0.5. Left column: PASI + log-law, right column: PASI + ODT. Results of PASI + log-law are equivalent to Bou-Zeid et al. [8]. Dashed lines correspond to the k^{-1} (blue) and $k^{-5/3}$ (red) slope.

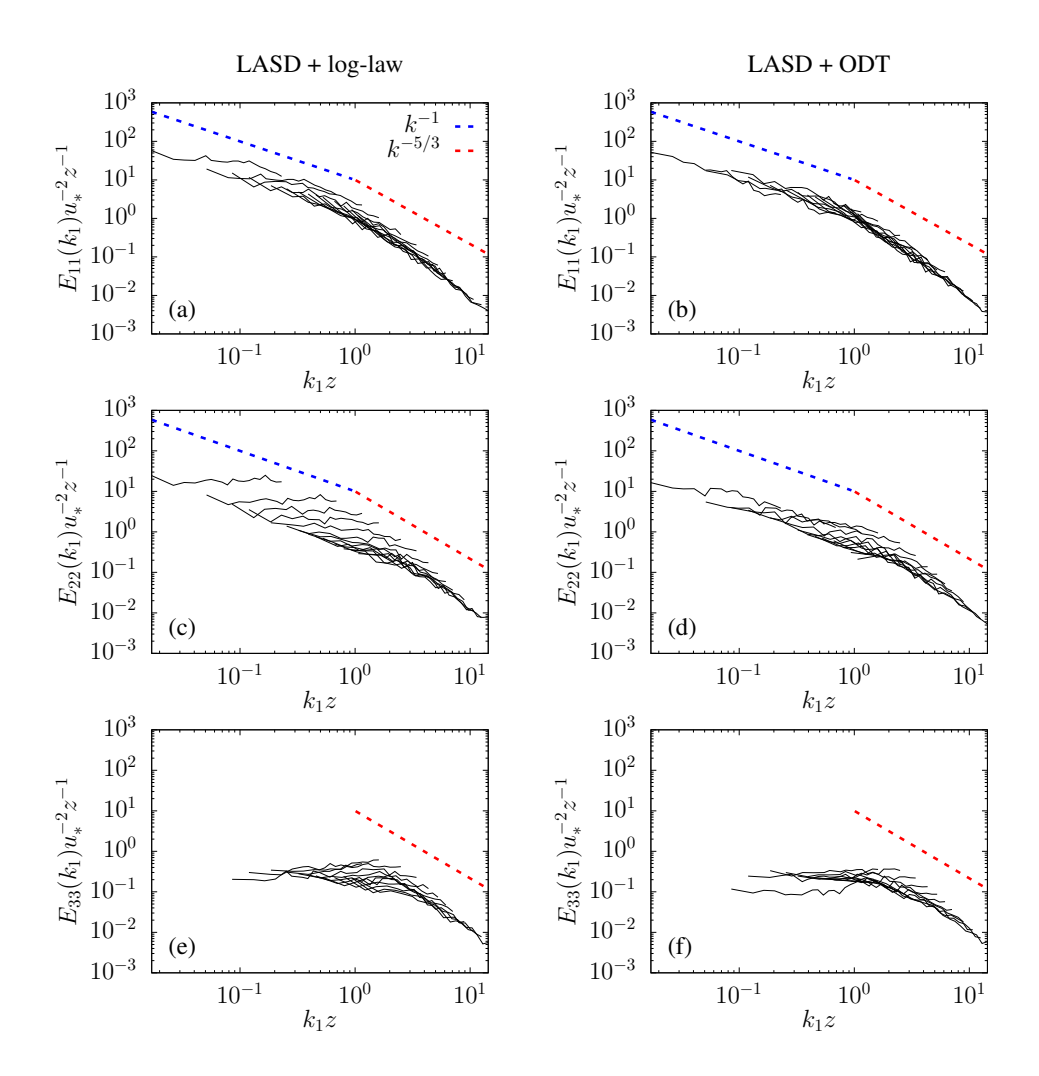


Figure 6: Same as Fig. 5 for LASD SGS model.

used in their study, the log-law is a type of Neumann boundary condition, and in our case a similar profile with a peak in the first grid was obtained. Sagaut [15, sec. 10.2.3] also mentions the issue of unphysical overshoots in the turbulence intensities near the wall for wall-modeled LES, which are caused by large spurious streaky structures that can be caused by a combination of mesh size and numerical methods. In the wall-resolved case of Bae et al. [36] using the no-slip boundary condition, a grid refinement allowed the formation, break-up and meandering of smaller streaks, improving the turbulence intensity statistics. A similar improvement is likely being provided by the wall-refined LES-ODT simulation compared to the LES + log-law, which has larger streaky structures (Fig. 7). Furthermore, in addition to mesh size and boundary condition, the wall blockage effect can cause the splatting of turbulent eddies coming from the outer part of the boundary layer, which can also be impacting the streaky structures [15, 36]. Bae et al. [36] observed an improvement when using the slip boundary condition with transpiration. Sagaut [15] mentions the possibility of use of random noise to scramble the spurious streamwise vortices, which is likely also being achieved by the stochastic nature of the ODT.

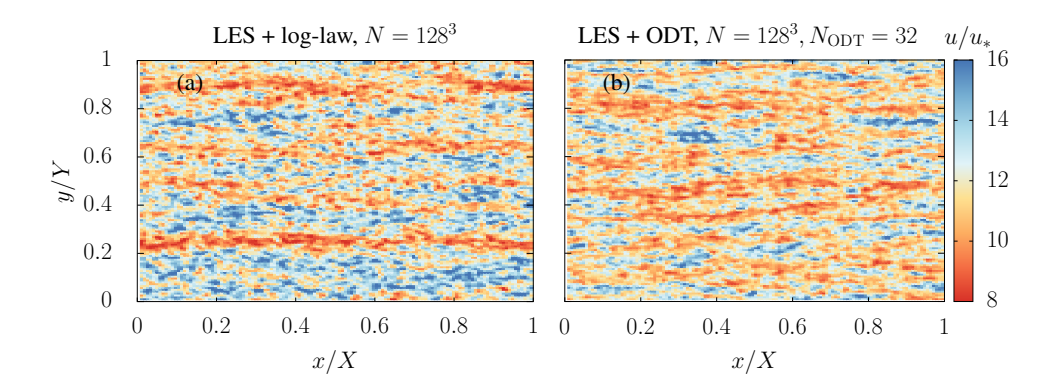


Figure 7: Wall-parallel snapshots of streamwise velocity at the second LES grid point in the rough channel simulations with 128³ grid points.

Figure 8 shows flow statistics for different combinations of grid points in the ODT (from 8 to 96, with LES grid fixed at 64^3) and in the LES (64^3 and 128^3 , with ODT grid fixed at 32). The final values of $\Delta t/\Delta t_{\rm ODT}$ were 15, 15, 30, 60, 120 for $N_{\rm ODT}=8,16,32,64,96$ respectivelly, indicating that the smaller the $\Delta z_{\rm ODT}$, the smaller the scale of the smallest stochastic eddy and therefore a smaller $\Delta t_{\rm ODT}$ is required, as expected. A convergence in the mean velocity profile for ODT grid points equal to 32 or more (Fig. 8a,c) indicates the success of the ODT SGS model (the small variability observed in the streamwise variance is intrinsic to the LES model). However, for $N_{\rm ODT}=16$ and 8, the stochastic eddies in ODT are likely not well resolved, resulting in an overestimation of the mean streamwise velocity in the LES domain (Fig. 8a) Therefore, a minimum of $N_{\rm ODT}=32$ is recommended and will be used throughout this study. The mean streamwise velocity is unaffected by the change in LES resolution (Fig. 8b), and the difference observed in velocity variances are also intrinsic to the LES (Fig. 8d, LES + log-law for $N=128^3$ is also shown for comparison), a feature that is not impacted by the ODT.

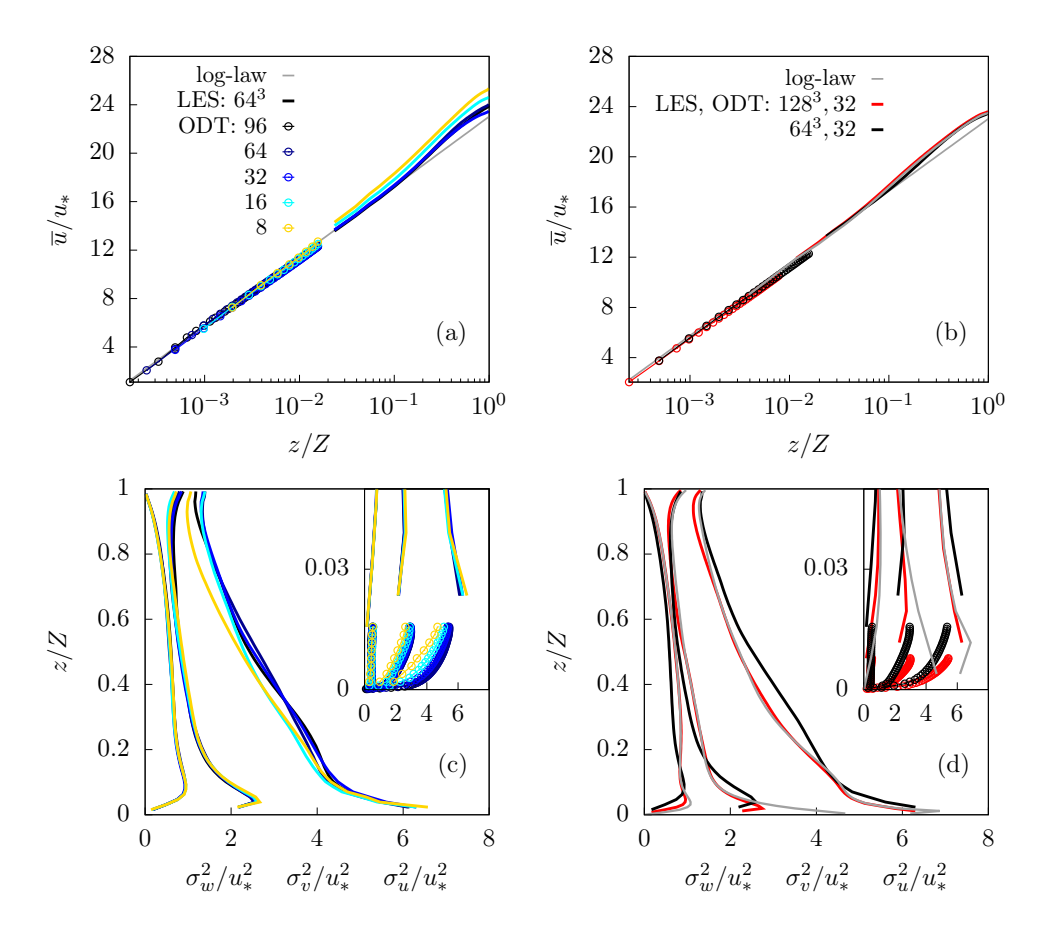


Figure 8: Sensitivity of LES-ODT simulation (LASD SGS model, $C_{\lambda}=15$) to grid resolution for the rough channel case (LES as solid lines and ODT as open circles): (a) and (b) mean streamwise velocity, (c) and (d) variances of streamwise (right), spanwise (middle) and vertical (left) velocities. Left panels: LES with 64³ grid points and ODT with 8 (yellow), 16 (cyan), 32 (blue), 64 (dark-blue) and 96 (black) grid points. Right panels: ODT with 32 grid points and LES with 64³ (black) and 128³ (red) grid points. In (b) and (d) grey lines correspond to LES + log-law with 128³ grid points.

4.2. Smooth channel

Figure 9 shows the statistics of the smooth channel simulations using the LASD SGS model. In these simulations, the first LES grid is in the transition between the viscous and the logarithmic layer, which is not captured by the LES+log-law by construction, as it assumes that the first LES grid point is in the logarithmic region. With the ODT wall model, on the other hand, there is no restriction on the distance of the LES grid points from the wall. They are similar to DNS results for both $Re_{\tau} = 590$ and 5200, using the same roughchannel parameter $C_{\lambda} = 15$, and selecting the second ODT parameter $Z_{\lambda} = 120$ (the viscous cutoff parameter) by trial-and-error. Variances in the ODT part of the simulation begin correctly in the viscous sublayer but evolve to a wrong shape and values around the peak, which was also observed in by Schmidt et al. [14]. Overall, variances in ODT stand-alone model have wrong values but the correct order of magnitude and overall behavior [18], which is also observed in LES-ODT. Some improvement in ODT variances when forced by LES, compared to ODT stand-alone, is discussed by Schmidt et al. [14]. Notice that the variances in LES are not impacted by ODT (they are similar to the LES + log-law results), except close to the wall especially for the spanwise variance, as observed in the rough-channel case. The ODT viscous stress is similar to DNS values, and *stochastic eddies* emulate the Reynolds stress in the viscous and buffer sublayers. The sum of them gives the correct total stress, which matches the linear profile in both ODT and LES parts, indicating a well developed, steady-state simulation.

The sensitivity of the simulation to the Z_{λ} parameter is small. By changing Z_{λ} from 100 to 140 there is a small change in mean streamwise velocity and variances (Fig. 10), and an almost imperceptible increase in the total stress at $z = \Delta z$, indicating the beginning of a deviation from the linear profile due to a Z_{λ} value that is too large (not shown). In comparison to the original LES-ODT coupling by Schmidt et al. [14], the smooth-channel results presented here are qualitatively similar with small differences likely due to differences in the LES codes.

4.3. Rough channel with drag force

In this section we analyse the LES-ODT simulation of a rough channel with an additional roughness modeled by a drag force close to the surface, comparing it with field data measured in a maize field during approximately neutral stability conditions [34]. This is an interesting case because there is both LES and ODT stand alone canopy-resolving simulations of the same case in the literature, by Pan et al. [24] and Freire and Chamecki [18], respectively. The same drag force model was used in all of these simulations, as proportional to the measured leaf area density and the square of the local velocity, with a constant drag coefficient. We note that Pan et al. [24] presents results with both constant and variable drag coefficients, the latter being closer to the field data, as it models the canopy ability to bend and reconfigurate. However, because the variable drag coefficient approach did not work in the ODT (it worsen the results [18]), we chose to reproduce here only the constant drag coefficient results from the LES canopy-resolving study, in order to obtain a direct comparison with the LES-ODT approach.

Statistics of the flow within and right above the canopy are similar to the ones obtained by ODT stand alone [18]. The mean velocity profile displays the correct shape when compared to field observations, despite overestimation (underestimation) within (above) the canopy

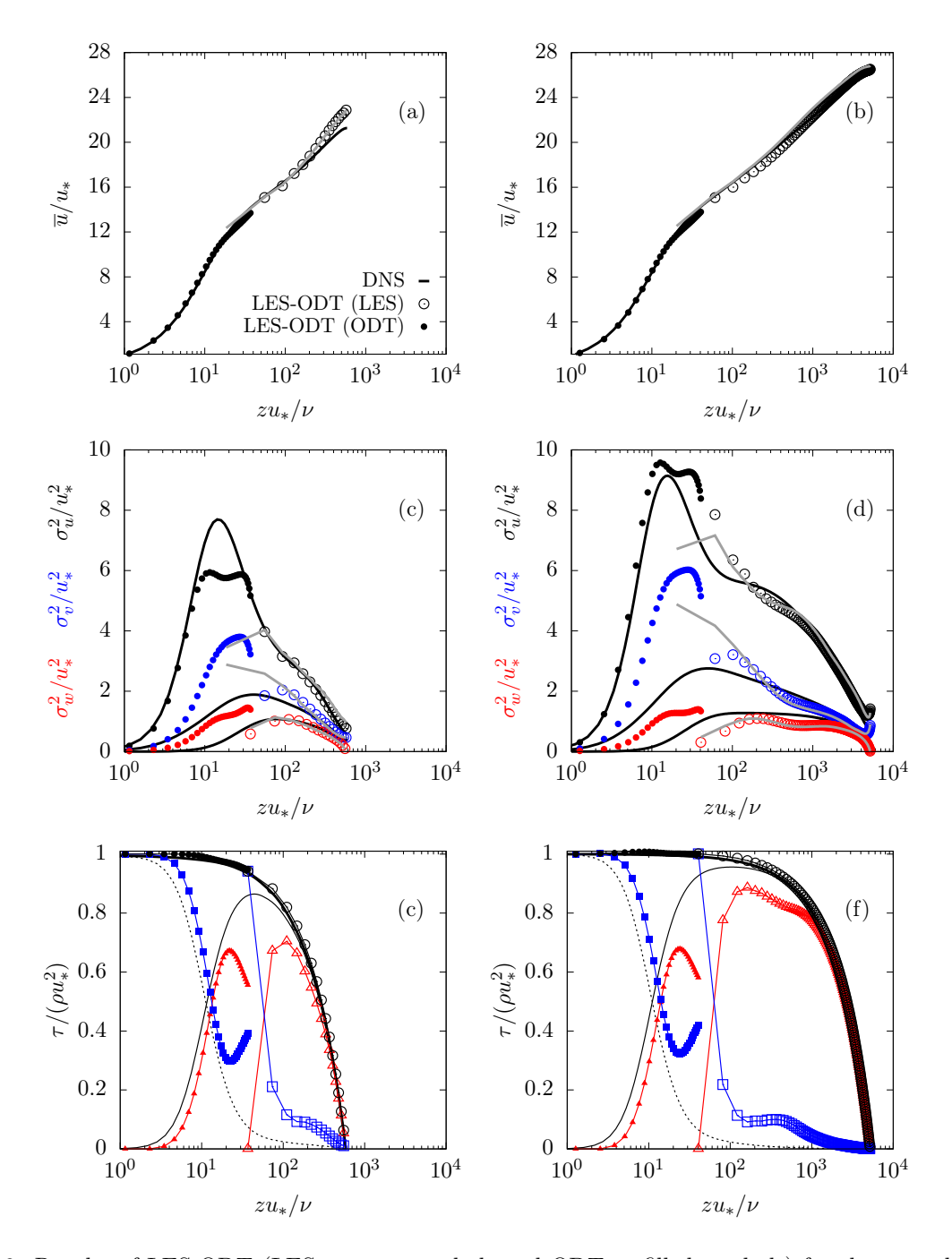


Figure 9: Results of LES-ODT (LES as open symbols and ODT as filled symbols) for the smooth channel case (LASD SGS model): (a, b) mean streamwise velocity, (c, d) variances of streamwise (black), spanwise (blue) and vertical (red) velocities, and (e, f) SGS (blue), resolved (red) and total (black) stress. Left and right panels correspond to $Re_{\tau}=590$ and 5200, respectively. Gray lines correspond to LES + log-law. Black lines correspond to DNS results by Moser et al. [33] (left panels) and Lee and Moser [32] (right panels), and in (e, f) it corresponds to the viscous stress (dotted lines), Reynolds stress (thin lines) and total stress (thick lines).

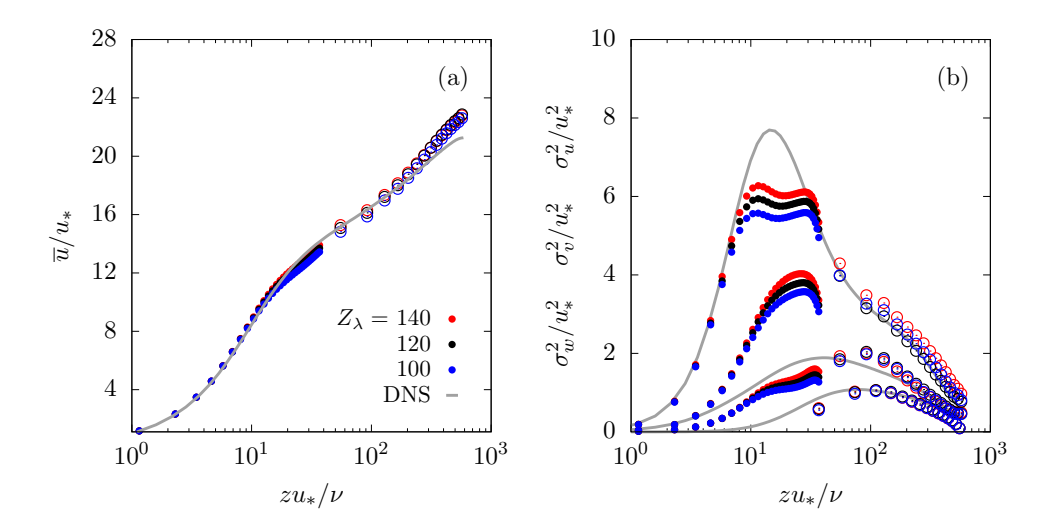


Figure 10: Sensitivity of simulation to Z_{λ} for the smooth channel case, LES (open circles) and ODT (filled circles): (a) mean streamwise velocity, (b) variances of streamwise (top), spanwise (middle) and vertical (bottom) velocities. Simulations with $Z_{\lambda} = 120$ (red), 98 (black) and 80 (blue). Grey lines correspond to DNS results by Moser et al. [33].

(Fig. 11a). Also similarly to ODT stand alone, velocity variances are underestimated above the canopy in the horizontal directions and underestimated both within and above the canopy in the vertical direction (Fig. 11b–d). This correspondence of flow statistics provides an opportunity to use the ODT stand alone model as a first test to estimate the potential of the LES-ODT coupling in representing near-wall features that are of interest for a given study.

538

539

540

542

543

544

545

546

547

549

550

551

553

554

555

556

557

558

559

560

561

562

An interesting result to notice is the skewness of streamwise (Sk_n) and vertical (Sk_n) velocities within the canopy, as they are a signature of the mixing-layer type vortices present in canopy flows [37]. By itself, ODT is able to produce a Sk_u profile with the correct sign and order of magnitude in the upper canopy (similar to Fig. 11), but it cannot produce Sk_w different from zero [18]. This is because in ODT the vertical velocity is simulated as a separate "scalar field", only connected to the streamwise velocity by the energy redistribution term (the only cause of the non-zero variances of spanwise and vertical velocities in ODT channel flows). The value of Sk_u , on the other hand, is a consequence of the inflection point in the streamwise velocity at canopy top. The non-zero value of Sk_w obtained in the LES-ODT simulation (Fig. 11h) is a clear evidence of the improvement in vertical velocity dynamics in the ODT driven by the LES. We note that the same value of Sk_w is obtained even if a one-way coupling is performed, i.e., in a simulation in which LES + log-law is used to drive ODT, but no ODT information is passed to LES (not shown). This means that this Sk_w value is a result of the near-wall three-dimensional dynamics of the LES flow, even if the LES does not "know" about the local inflection point caused by the drag force. We also note that in the canopy-resolving LES the value of Sk_w is smaller than in the field data (Fig. 11h), indicating that this dynamics of the flow is difficult to be captured even in LES. This result reinforces the ODT ability in capturing some important flow characteristics when driven by the LES.

For the remaining of the domain above the canopy, the LES-ODT results are similar to LES + log-law with an enhanced roughness height parameter (Fig. 12), with the exception of

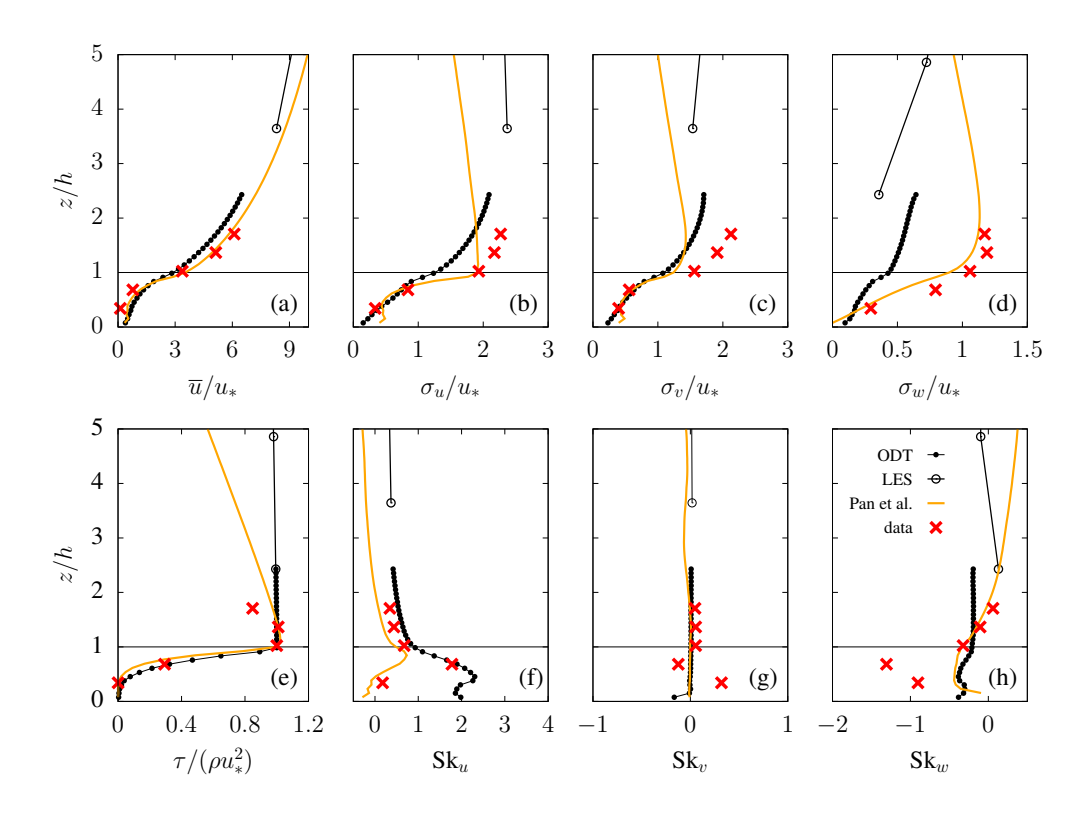


Figure 11: Results of LES-ODT (LES as open circles and ODT as filled circles) for the channel with maize field looking close to the canopy region ($h=2.1\,\mathrm{m}$ is the canopy height): (a) mean streamwise velocity, variances of (b) streamwise, (c) spanwise and (d) vertical velocities, (e) total stress and skewness of (f) streamwise, (g) spanwise and (h) vertical velocities. Orange lines correspond to LES canopy-resolving simulation by Pan et al. [24] and crosses correspond to field data from Gleicher et al. [34].

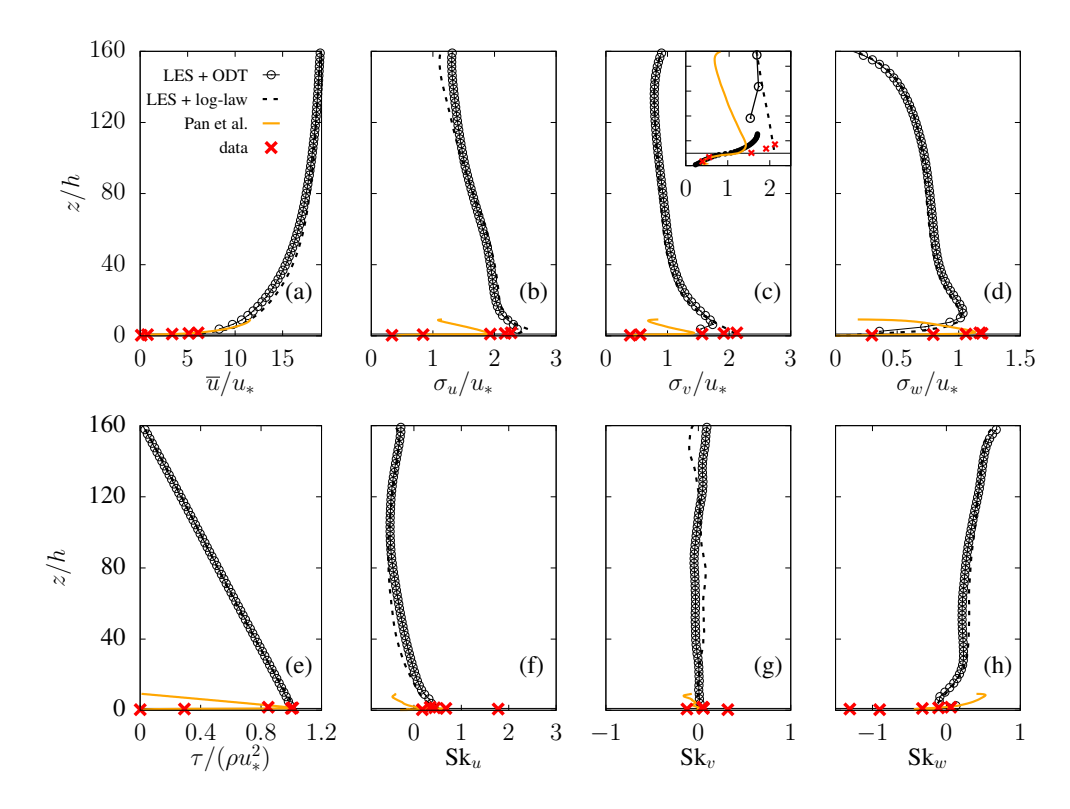


Figure 12: Same as Fig. 11 for the entire vertical domain.

the spanwise velocity near the wall as observed in previous cases. Finally, it is important to point out that any canopy-resolving LES, as performed by Pan et al. [24], has a computational cost that restricts the domain size significantly (see the size of the domains in Fig. 12 for comparison). Despite the additional computational cost, the LES-ODT coupling allows a bigger domain, which can be useful in studies of the entire atmospheric boundary layer with important near-wall phenomena.

4.4. Computational cost

As discussed in details by Schmidt et al. [14], the computational cost of the ODT is highly variable. It depends not only on the number of ODT models $(N_x \times N_y)$ and the number of ODT grid points $(N_{\rm ODT})$, but it also depends on the intensity and scales of turbulence being simulated by ODT, which impact the number of ODT time steps within one LES time step $(\Delta t/\Delta t_{\rm ODT})$. In their study, the computational cost of the smooth channel flow (which is a "wall-resolved" case) was estimated as scaling with $Re_{\tau}^{2.3}$ approximately. Fig. 13 provides the CPU time spent in the rough-channel simulations, which is "wall-modeled" and does not scale with Re_{τ} (the simulation of maize field has a similar computational cost). To avoid differences across specific runs due to the instability of the cluster, the CPU time was estimated as the ensamble average of 3 realizations of 100 time steps at the end of each simulation. The computational cost of the LES-ODT with $N_{\rm ODT}=32$ ($\Delta t/\Delta t_{\rm ODT}=30$) is about one order of magnitude higher than the LES + log-law with the same resolution (Fig. 13a), showing that the ODT part corresponds to the majority of the computational cost of the simulation. As a consequence, the cost also increases significantly when increasing

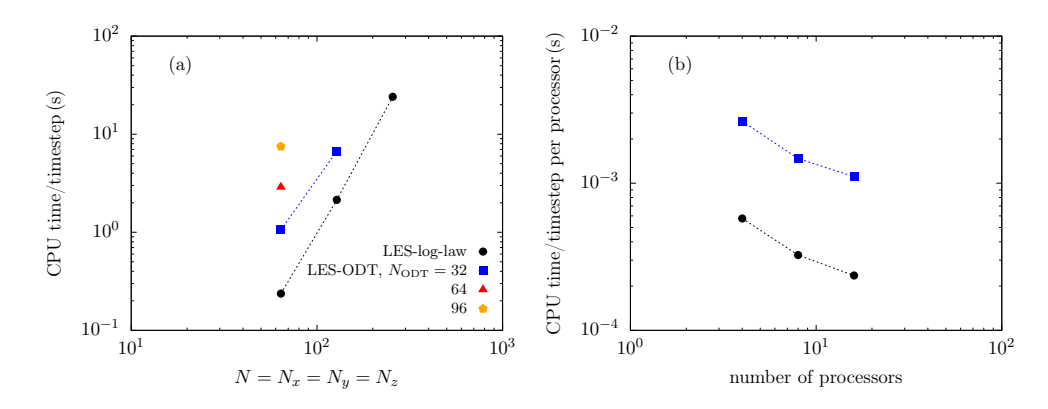


Figure 13: (a) CPU time per time step as a function of the number of LES grid points in any direction. (b) CPU time per time step per processor as a function of number of processors for $N=64, N_{\rm ODT}=32$. LES + log-law (black circles), LES-ODT with $N_{\rm ODT}=32$ (blue squares), 64 (red triangle) and 96 (orange pentagon).

 $N_{\rm ODT}$ to 64 ($\Delta t/\Delta t_{\rm ODT}=60$) and 96 ($\Delta t/\Delta t_{\rm ODT}=120$) (Fig. 13a), which is caused not only by the increase in $N_{\rm ODT}$ but also the decrease in $\Delta t_{\rm ODT}$. By increasing $N_x=N_y=N_z$ from 64 to 128, the increase in LES-ODT computational cost has a slightly lower rate than LES + log-law. The decrease in cost per processor, on the other hand, has a slightly higher rate compared to LES + log-law (Fig. 13b), indicating that the parallelization of the ODT was successful. Therefore, LES-ODT provides a good scalability for larger domains.

585

586

587

588

589

590

591

592

593

594

595

596

597

598

599

600

601

602

603

604

605

606

607

608

609

610

611

612

The LES-ODT cost is significantly high compared to LES alone. However, for a LES code with fixed-grid, this approach provides a high-resolution flow close to the wall with an affordable computational cost, representing an alternative for studies in which the flow in the first LES grid needs high resolution, but not in the remaining LES domain. To provide a visualization of this potential trade-off, we compare the simulation of LES-ODT with 128³ grid points and $N_{\rm ODT}=32$ with LES + log-law of 128^3 and 256^3 . Note that the LES-ODT has a computational cost in between the two LES + log-law's (Fig. 13a), and that the LES + log-law with 256³ needs to run with half Δt and double number of time steps due to the grid refinement. Figure 2 shows an example of snapshots of these simulations. It is clear that the LES-ODT reproduces the overall flow scales of the LES + log-law with the same resolution, but near the wall it also provides additional representation of small scales comparable to the LES with higher resolution. Figure 14 compares the one-dimensional spectra at the same heights, in which the same benefits discussed in Sec. 4.1 are still present, especially the improvement in spanwise spectra near the wall. While in the LES + log-law with 256³ the lowest available flow fields are at z/Z = 0.002 and 0.006, in the LES-ODT one would have in this case instantaneous flow from z/Z = 0.00025 to 0.008 at 0.00025 intervals (see Fig. 2). Figure 15a compares a snapshot of the streamwise velocity in the wall-parallel layer at z/Z = 0.002, showing that LES-ODT captures some important features of the flow, such as the overall shape and intensity of turbulence structures. Furthermore, away from the wall the flow is dominated by large-scale structures, and the gain in flow resolution is likely less relevant (Fig. 15b). Therefore, despite its high computational cost for a wall model, LES-ODT might be seen as an alternative approach for near-wall resolution, which can be useful for studies in which a instantaneous flow field near the wall is required, such as canopy

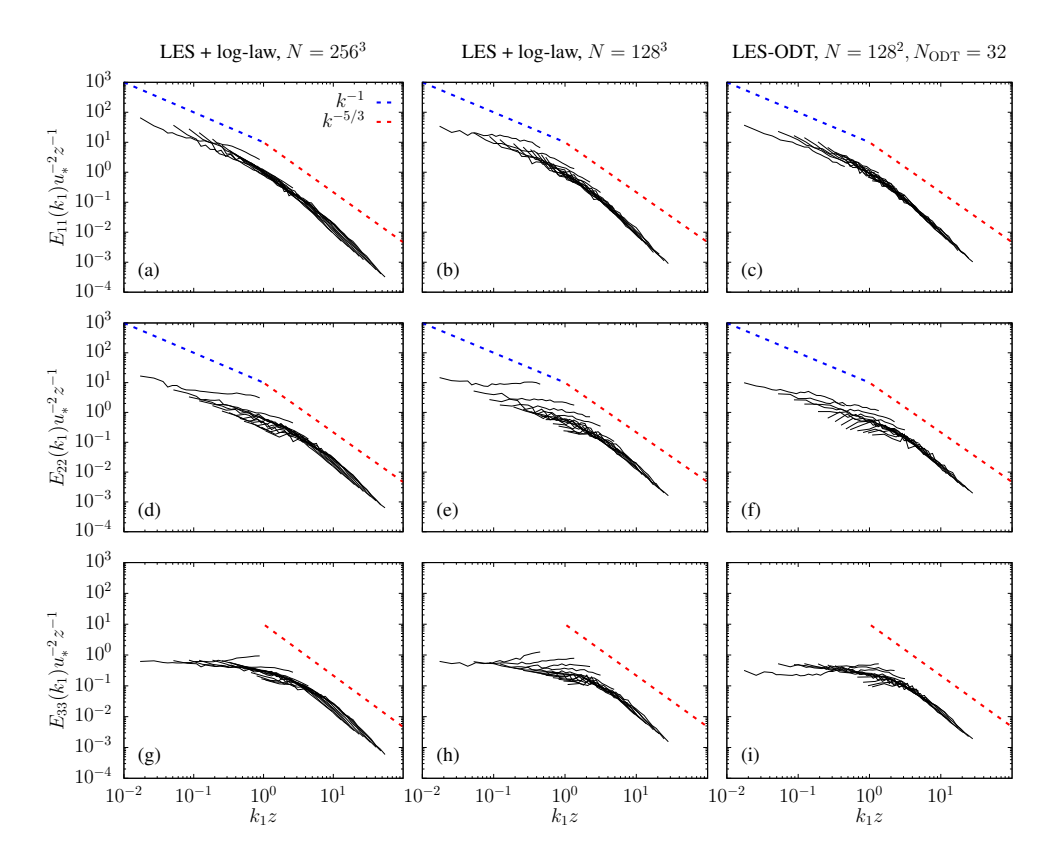


Figure 14: One-dimensional spectra of (a,b,c) streamwise, (d,e,f) spanwise and (g,h,i) vertical velocity, for the same heights z/Z from 0.008 to 0.5. Left and middle columns: LASD + log-law with 256³ (left) and 128³ (middle) grid points, right column: LASD + ODT with $N = 128^3$, $N_{\rm ODT} = 32$ grid points. Dashed lines correspond to the k^{-1} (blue) and $k^{-5/3}$ (red) slope.

614 flows and sediment transport.

5. Summary and conclusions

In this study, we develop a new stochastic wall-model based on the "large-eddy" version of ODT, testing it for rough and smooth channel flows. An extensive discussion regarding the ability of ODT in representing turbulent flows is provided in the original study of LES-ODT coupling [14] and in several others ODT stand-alone studies [16, 17, 18], and it can be summarized as follows. In general, ODT provides a useful representation of a non-equilibrium turbulent flow in one dimension, with one adjustable parameter (or two if a viscous sublayer is resolved) that has a value in the order of 10 (viscous parameter in the order of 100), but that can be tuned for a specific benchmark result before extrapolating to blind test scenarios, including different Reynolds number, domain size and model resolution. This parameter is tuned to adjust the mean flow, providing variances that are not strictly correct, but that typically has the correct overall shape and order of magnitude. In the example of channel flow, the parameter is adjusted to match the log-law behavior, and it is valid for smooth and rough channels, in addition to the atmospheric boundary layer under different conditions (such as different atmospheric stabilities [18]). When coupled to LES, ODT behaves as a wall model that not only improves the LES flow field close to the wall, but also provides

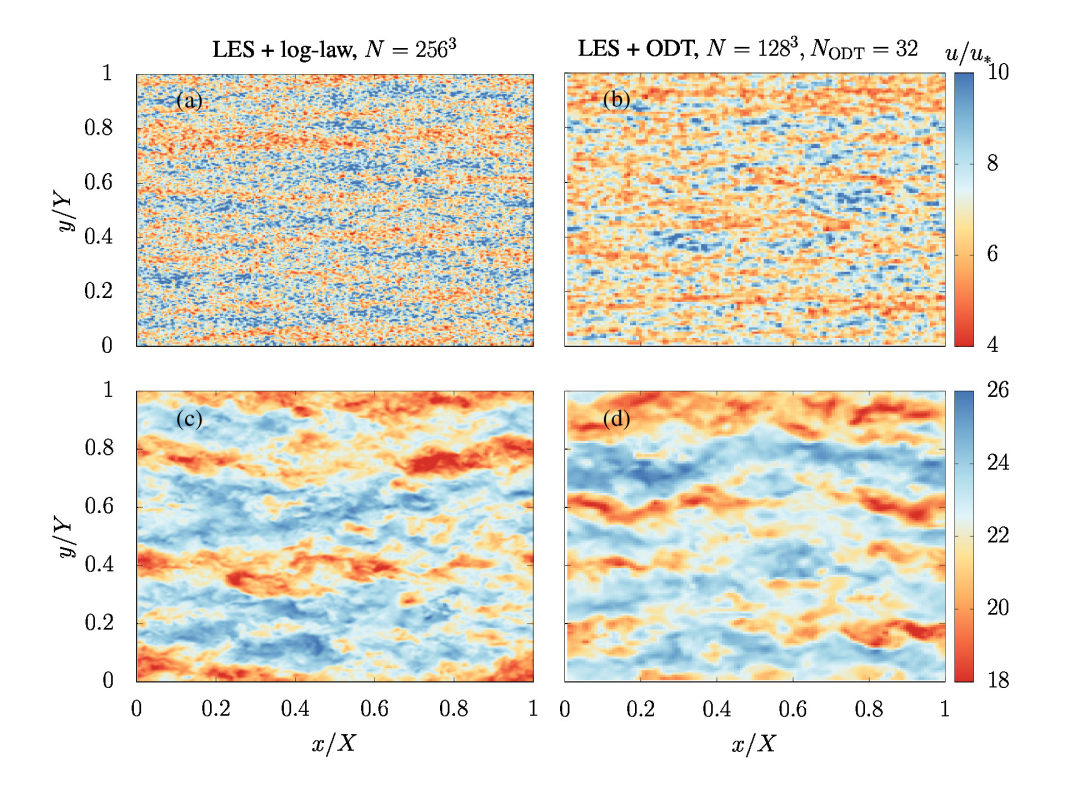


Figure 15: Snapshots of the streamwise velocity in the horizontal plane at z/Z = 0.002, for (a,c) LES + log-law with $N = 256^3$ and (b,d) LES-ODT with $N = 128^3$, $N_{\rm ODT} = 32$.

near-wall vertically-refined instantaneous flow field that can be useful in many applications. Due to its formulation based on the diffusion equation, other variables can be incorporated to the ODT and coupled to the LES in a similar way to what is typically done in LES alone (including temperature and scalar concentration, buoyancy effects, sources and sinks, and so on).

From the results presented here, two important conclusions can be drawn: (i) replacing the wall model from the log-law to ODT improves the energy spectrum for both SGS models tested here (PASI and LASD). Near the wall, the improvement is in the entire range of resolved scales (not only in the smaller scales), producing a much clearer k^{-1} scaling in the production range. For the PASI case, the improvement also fixes the mean velocity gradient mismatch present when the log-law boundary condition is used. Therefore, coupling ODT makes the flow field of LES in the first grid points more realistic than using the log-law. (ii) If we take the traditional dynamic model (PASI) as a reference, using ODT as a wall model is more advantageous than improving the SGS model to LASD. Nevertheless, the use of LASD and ODT can be useful for the study of heterogeneous problems, since it does not rely on planar averages as the original PASI method.

Overall, the decision of using the LES-ODT approach should focus on the balance between the advantages of ODT and its computational cost. Currently, most of the LES-ODT cost comes from the ODT alone. Because this study did not focus on numerical performance, this is an aspect that has room for future improvement. Note that the spectral method is not required for the LES-ODT approach *per se*, it is specific for the LES code used in this

study. Future studies could test this approach using different codes, including other versions of the ODT model such as with an adaptative mesh and cylindrical/spherical formulations [38]. Regarding its advantages, the LES-ODT coupling may provide an useful alternative for studies that rely significantly on the turbulence near the wall, and that cannot afford to perform the grid refinement necessary in LES alone. It is particularly encouraging given the improvement in spanwise and vertical velocity dynamics of the ODT driven by the LES, as evidenced by the presence of vertical velocity skewness within the canopy simulated by the ODT, which cannot be achieved by the ODT stand-alone model. Furthermore, ODT stand alone can be used beforehand to assess the ODT ability in represent the phenomenon of interest. Note that the overall behavior of the ODT is not expected to be LES-dependent, it is similar to its stand-alone results, with some improvement related to the large-scale forcing (see the ODT versus LES-ODT comparison in Schmidt et al. [14]). For a comparison to other types of wall models, the reader is also referred to a detailed discussion present in Schmidt et al. [14].

Examples of studies that can benefit from the LES-ODT coupling are environmental and geophysical flows with relevant near-wall dynamics, such as the atmospheric boundary layer in the presence of canopy, sediment transport in the atmosphere and rivers, snow drift, and many others. Because each ODT behaves as an independent model, whose domain is a horizontally-homogeneous sub-domain (affected by large-scale advection), each ODT can also be used to represent horizontal heterogeneity at the surface, such as the presence of different obstacles, surface roughness, and so on. The model might be particularly relevant for studies with convective turbulence, as they typically require large domains needed to simulate the large-scale turbulence structures. Therefore, the next step will be to implement and test buoyancy effects in the LES-ODT coupling, in addition to an effort in reducing its computational cost.

677 Acknowledgement

L.S.F. was funded by the São Paulo Research Foundation (FAPESP, Brazil), Grants No. 2018/24284-1 and 2019/14371-7. MC was supported by National Science Foundation Grant AGS1358593. Research carried out using the computational resources of the Center for Mathematical Sciences Applied to Industry (CeMEAI) funded by FAPESP (grant 2013/07375-0). We thank Bicheng Chen and Tomas Chor for discussion and assistance with the LES code, and Leonardo Martinussi and Leandro Franco de Souza for technical support.

684 Appendix A.

The size of the overlap region is one of the parameters that impact the result of the LES-ODT coupling. Ideally, it should provide the appropriate transition between the sizes of the largest stochastic eddies in ODT and smallest resolved eddies in LES. In the original study, Schmidt et al. [14] tested the effect of this parameter and found that $l_{\text{max}} = 3.5\Delta z$ was an appropriate size for the largest stochastic eddies. We reproduced this result in our code to ensure that their finding is consistent, which is presented in Fig. A.16. As in the original study, the changes in the mean velocity when varying l_{max} from 2.5 to 3.5 are larger than when changing l_{max} from 3.5 to 4.5 Δz , indicating that for $3.5\Delta z$ provides some sort of saturation level and is therefore the appropriate value.

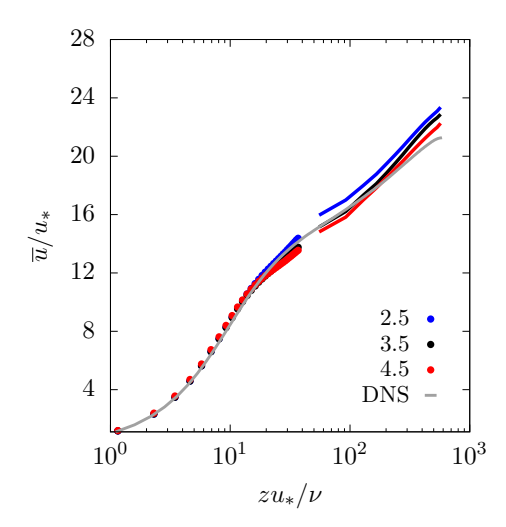


Figure A.16: Smooth channel flow results for for different values of the largest stochastic eddy l_{max} ($Re_{\tau} = 590$).

f Appendix B.

695

696

697

698

699

700

702

703

704

705

706

707

708

709

710

711

712

713

714

715

716

717

718

719

An important detail of the LES-ODT coupling regarding the LES resolved and SGS momentum fluxes deserves clarification. By construction, the LES stresses at the wall and at $z = \Delta z$ (top of the lowest grid) come from ODT only. Because they enter as SGS stresses, the resolved stress at those points should be zero (as shown in Fig. 3c,f). However, because LES velocities at the lowest LES grid comes from ODT through the averaged ODT velocities \tilde{v}_i , the covariance $\tilde{v}_{i=1,2}\tilde{v}_3$ is actually different from zero at $z = \Delta z$. This is a consequence of the estimation of \tilde{v}_3 from $\tilde{v}_{i=1,2}$ to enforce continuity (Eq. 15). In order to ensure that the ODT stress is the total stress, this non-zero resolved stress in the LES is not used in the calculation of the resolved advection term (as if it was zero). This causes the simulation equilibrium to be achieved with a stress that has a local peak at $z = \Delta z$ (see Fig. B.17). But the real equilibrium stress "known" to the LES is the linear one presented in Fig. 3, which is obtained by assuming $\tilde{v}_{i=1,2}\tilde{v}_3$ at $z = \Delta z$ equal to zero in the plot. If this non-zero value is taken into account by the LES advection calculation, the equilibrium simulation is different from the log-law due to a mismatch between the velocity and stress imposed in the LES from the ODT.

Another consequence of this non-zero $\widetilde{v}_{i=1,2}\widetilde{v}_3$ at $z=\Delta z$ is that the value of the resolved stress (or Leonard stress) L_{ij} of the dynamic model is non-zero at $z=\Delta z$ when it should be zero. For the PASI SGS model this is not an issue because this value would only impact the velocity field in the first grid (due to the planar averaging approach), but this velocity is replaced by the ODT value. For the LASD SGS model, on the other hand, this value can influence the velocity field in other heights due to the Lagrangian averaging, therefore it has to be set to zero in order to generate the correct SGS modeling.

References

Numerical Υ. Tsuji, evidence logarithmic Yamamoto, of rein channel flow Re_{τ} 8000, Physical Review Flugions at

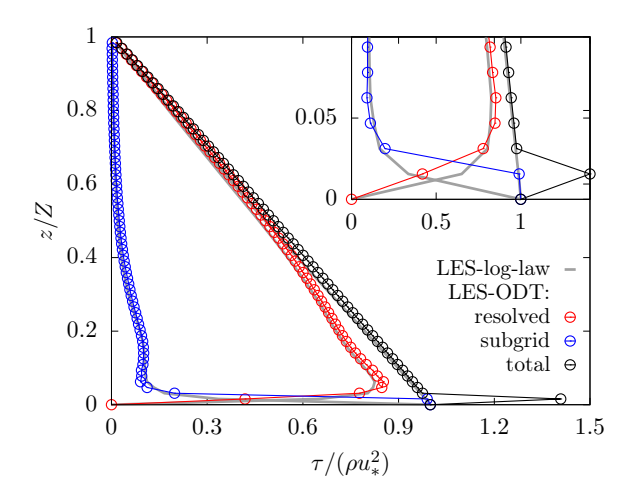


Figure B.17: Resolved (red), SGS (blue) and total (black) stress as obtained from the LES. The point out of the linear curve is caused by the non-zero resolved stress at $z = \Delta z$ that is not taken into account by the simulation due to the LES-ODT coupling formulation.

- ids 3 (2018) 012602, doi:10.1103/PhysRevFluids.3.012602, URL https://link.aps.org/doi/10.1103/PhysRevFluids.3.012602.
- [2] T. S. Lund, X. Wu, K. D. Squires, Generation of Turbulent Inflow Data for Spatially-Developing Boundary Layer Simulations, Journal of Computational Physics 140 (2) (1998) 233 - 258, ISSN 0021-9991, doi:https://doi.org/10.1006/jcph.1998.5882, URL http://www.sciencedirect.com/science/article/pii/S002199919895882X.
- To Voelkl, D. I. Pullin, D. C. Chan, A physical-space version of the stretched-vortex subgrid-stress model for large-eddy simulation, Physics of Fluids 12 (7) (2000) 1810–1825, doi:10.1063/1.870429, URL https://doi.org/10.1063/1.870429.
- [4] P. Schlatter, Q. Li, G. Brethouwer, A. V. Johansson, D. S. Henningson, Simulations of spatially evolving turbulent boundary layers up to Re_{θ} =4300, International Journal of Heat and Fluid Flow 31 (3) (2010) 251 261, ISSN 0142-727X, doi:https://doi.org/10.1016/j.ijheatfluidflow.2009.12.011, URL http://www.sciencedirect.com/science/article/pii/S0142727X09001763, sixth International Symposium on Turbulence and Shear Flow Phenomena.
- [5] S. Ryu, G. Iaccarino, A subgrid-scale eddy-viscosity model based on the volumetric strain-stretching, Physics of Fluids 26 (6) (2014) 065107, doi:10.1063/1.4882880, URL https://doi.org/10.1063/1.4882880.
- [6] S. Khanna, J. G. Brasseur, Analysis of MoninObukhov similarity from large-eddy simulation, Journal of Fluid Mechanics 345 (1997) 251286, doi:10.1017/S0022112097006277, URL http://dx.doi.org/10.1017/S0022112097006277.
- [7] Y. Noh, W. G. Cheon, S. Y. Hong, S. Raasch, Improvement of the K-profile Model for
 the Planetary Boundary Layer based on Large Eddy Simulation Data, Boundary-Layer

- Meteorology 107 (2) (2003) 401–427, ISSN 1573-1472, doi:10.1023/A:1022146015946, URL https://doi.org/10.1023/A:1022146015946.
- [8] E. Bou-Zeid, C. Meneveau, M. Parlange, A scale-dependent Lagrangian dynamic model for large eddy simulation of complex turbulent flows, Physics of Fluids 17 (2) 025105, doi:10.1063/1.1839152, URL http://dx.doi.org/10.1063/1.1839152.
- [9] U. Piomelli, Wall-layer models for large-eddy simulations, 748 Aerospace 437 **ISSN** Progress in Sciences 44 (6)(2008)446, 749 doi:https://doi.org/10.1016/j.paerosci.2008.06.001, URL 0376-0421, 750 http://www.sciencedirect.com/science/article/pii/S037604210800047X, large 751 Eddy Simulation - Current Capabilities and Areas of Needed Research. 752
- 753 [10] J. Larsson, S. Kawai, J. Bodart, I. Bermejo-Moreno, Large eddy simulation 754 with modeled wall-stress: recent progress and future directions, Mechanical Engi-755 neering Reviews 3 (1) (2016) 15–00418–15–00418, doi:10.1299/mer.15-00418, URL 756 http://dx.doi.org/10.1299/mer.15-00418.
- [11] J. Lee, M. Cho, H. Choi, Large eddy simulations of turbulent channel and boundary layer flows at high Reynolds number with mean wall shear stress boundary condition, Physics of Fluids 25 (11) (2013) 110808, doi:10.1063/1.4819342, URL https://doi.org/10.1063/1.4819342.
- [12] S. Τ. Bose, G. I. Park, Wall-Modeled Large-Eddy Simulation 761 Turbulent for Complex Flows. Annual Review Fluid Mechanics 762 50 (2018)doi:10.1146/annurev-fluid-122316-045241, URL 535–561. 763 https://doi.org/10.1146/annurev-fluid-122316-045241. 764
- [13] E. Balaras, C. Benocci, U. Piomelli, Two-layer approximate boundary conditions for large-eddy simulations, AIAA Journal 34 (6) (1996) 1111–1119, ISSN 0001-1452, doi: 10.2514/3.13200, URL http://dx.doi.org/10.2514/3.13200.
- [14] R. C. Schmidt, A. R. Kerstein, S. Wunsch, V. Nilsen, Near-wall LES closure based on one-dimensional turbulence modeling, Journal of Computational Physics 186 (1) (2003) 317–355, ISSN 0021-9991, doi:10.1016/S0021-9991(03)00071-8, URL http://dx.doi.org/10.1016/S0021-9991(03)00071-8.
- [15] P. Sagaut, Large Eddy Simulation for Incompressible Flows, Springer, 3rd edn., 2006.
- 773 [16] A. Kerstein, W. T. Ashurst, S. Wunsch, V. Nilsen, One-dimensional turbulence: vector formulation and application to free shear flows, Journal of Fluid Mechanics 447 (2001) 85–109, ISSN 1469-7645, doi:10.1017/S0022112001005778, URL http://dx.doi.org/10.1017/S0022112001005778.
- T. Echekki, A. R. Kerstein, T. D. Dreeben, J.-Y. Chen, One-dimensional turbulence simulation of turbulent jet diffusion flames: model formulation and illustrative applications, Combustion and Flame 125 (3) (2001) 1083–1105, ISSN 0010-2180, doi:10.1016/S0010-2180 (01)00228-0, URL http://dx.doi.org/10.1016/S0010-2180 (01)00228-0.

- [18] L. S. Freire, M. Chamecki, A one-dimensional stochastic model of turbulence within and above plant canopies, Agricultural and Forest Meteorology 250–251 (2018) 9–23, ISSN 0168-1923, doi:10.1016/j.agrformet.2017.12.211, URL https://doi.org/10.1016/j.agrformet.2017.12.211.
- 785 [19] J. Kleissl, V. Kumar, C. Meneveau, M. B. Parlange, Numerical study of dynamic Smagorinsky models in large-eddy simulation of the atmospheric boundary layer: Validation in stable and unstable conditions, Water Resources Research 42 (6) (2006) W06D09, ISSN 1944-7973, doi:10.1029/2005WR004685, URL http://dx.doi.org/10.1029/2005WR004685.
- [20] M. Calaf, C. Meneveau, J. Meyers, Large eddy simulation study of fully developed wind-turbine array boundary layers, Physics of Fluids 22 (1) (2010) 015110, doi: 10.1063/1.3291077, URL http://dx.doi.org/10.1063/1.3291077.
- [21] L. S. Freire, M. Chamecki, J. A. Gillies, Flux-Profile Relationship for Dust Concentration in the Stratified Atmospheric Surface Layer, Boundary-Layer Meteorology 160 (2) (2016) 249–267, ISSN 1573-1472, doi:10.1007/s10546-016-0140-2, URL http://dx.doi.org/10.1007/s10546-016-0140-2.
- Mixed Layer: Recent Developments Enabled by Large Eddy Simulations, Reviews of Geophysics 57 (4) (2019) 1338–1371, doi:10.1029/2019RG000655, URL https://agupubs.onlinelibrary.wiley.com/doi/abs/10.1029/2019RG000655.
- [23] S. Dupont, G. Bergametti, B. Marticorena, S. Simoëns, Modeling saltation intermittency, Journal of Geophysical Research: Atmospheres 118 (13) (2013) 7109-7128, ISSN 2169-8996, doi:10.1002/jgrd.50528, URL http://dx.doi.org/10.1002/jgrd.50528.
- Y. Pan, M. Chamecki, S. A. Isard, Large-eddy simulation of turbulence and particle dispersion inside the canopy roughness sublayer, Journal of Fluid Mechanics 753 (2014) 499–534, ISSN 1469-7645, doi:10.1017/jfm.2014.379, URL http://dx.doi.org/10.1017/jfm.2014.379.
- A. R. Kerstein, One-dimensional turbulence: model formulation and application to homogeneous turbulence, shear flows, and buoyant stratified flows, Journal of Fluid Mechanics 392 (1999) 277–334, ISSN 1469-7645, doi:10.1017/S0022112099005376, URL http://dx.doi.org/10.1017/S0022112099005376.
- 812 [26] A. R. Kerstein, S. Wunsch, Simulation of a Stably Stratified Atmospheric Boundary Layer Using One-Dimensional Turbulence, Boundary-Layer Meteorol-814 ogy 118 (2) (2006) 325–356, ISSN 0006-8314, doi:10.1007/s10546-005-9004-x, URL 815 http://dx.doi.org/10.1007/s10546-005-9004-x.
- 816 [27] G. Sun, D. O. Lignell, J. C. Hewson, C. R. Gin, Particle dispersion in homogeneous tur-817 bulence using the one-dimensional turbulence model, Physics of Fluids 26 (26) 103301, 818 doi:10.1063/1.4896555, URL http://dx.doi.org/10.1063/1.4896555.

- 819 [28] M. Klein, H. Schmidt, Stochastic Modeling of Turbulent Scalar Trans-820 port at Very High Schmidt Numbers, Proceedings in Applied Mathemat-821 ics and Mechanics 17 (1) (2018) 639-640, doi:10.1002/pamm.201710289, URL 822 https://onlinelibrary.wiley.com/doi/abs/10.1002/pamm.201710289.
- [29] X. I. A. Yang, G. I. Park, P. Moin, Log-layer mismatch and modeling of the fluctuating wall stress in wall-modeled large-eddy simulations, Phys. Rev. Fluids 2 (2017) 104601, doi:10.1103/PhysRevFluids.2.104601, URL https://link.aps.org/doi/10.1103/PhysRevFluids.2.104601.
- [30] M. Germano, U. Piomelli, P. Moin, W. H. Cabot, A dynamic subgrid-scale eddy viscosity model, Physics of Fluids A 3 (7) (1991) 1760–1765, doi:10.1063/1.857955, URL http://dx.doi.org/10.1063/1.857955.
- [31] T. A. Zang, On the rotation and skew-symmetric forms for incompressible flow simulations, Applied Numerical Mathematics 7 (1) (1991) 27 – 40, ISSN 0168-9274, doi:https://doi.org/10.1016/0168-9274(91)90102-6, URL http://www.sciencedirect.com/science/article/pii/0168927491901026.
- 834 [32] M. Lee, R. D. Moser, Direct numerical simulation of turbulent channel flow up to Re_{τ} ≈ 5200 , Journal of Fluid Mechanics 774 (2015) 395–415, doi:10.1017/jfm.2015.268, URL http://dx.doi.org/10.1017/jfm.2015.268.
- [33] R. D. Moser, J. Kim, N. N. Mansour, Direct numerical simulation of turbulent channel flow up to $Re_{\tau}=590$, Physics of Fluids 11 (4) (1999) 943–945, doi:10.1063/1.869966, URL http://dx.doi.org/10.1063/1.869966.
- [34] S. C. Gleicher, M. Chamecki, S. A. Isard, Y. Pan, G. G. Katul, 840 three-dimensional spore concentration measurements and escape 841 fraction in a crop canopy using a coupled Eulerian-Lagrangian stochas-842 model, Agricultural and Forest Meteorology 194 (2014)118-131, tic **ISSN** doi:http://dx.doi.org/10.1016/j.agrformet.2014.03.020, URL 844 http://www.sciencedirect.com/science/article/pii/S0168192314000884. 845
- R. Stevens, M. Wilczek, C. Meneveau, Large-eddy simulation study of the logarithmic law for second- and higher-order moments in turbulent wall-bounded flow,
 Journal of Fluid Mechanics 757 (2014) 888907, doi:10.1017/jfm.2014.510, URL
 http://dx.doi.org/10.1017/jfm.2014.510.
- J. A. Lozano-Durán, S. T. Bose, Р. Moin, Turbulence |36| H. Bae. in-850 tensities in large-eddy simulation of wall-bounded flows, Physical Re-851 view Fluids 3 (2018)014610,doi:10.1103/PhysRevFluids.3.014610, URL 852 https://link.aps.org/doi/10.1103/PhysRevFluids.3.014610. 853
- In Finnigan, Turbulence in Plant Canopies, Annual Review of Fluid Mechanics 32 (1) (2000) 519–571, doi:10.1146/annurev.fluid.32.1.519, URL http://dx.doi.org/10.1146/annurev.fluid.32.1.519.

[38] D. O. Lignell, V. B. Lansinger, J. Medina, M. Klein, A. R. Kerstein, H. Schmidt,
 M. Fistler, M. Oevermann, One-dimensional turbulence modeling for cylindrical and
 spherical flows: model formulation and application, Theoretical and Computational
 Fluid Dynamics 32 (4) (2018) 495–520, ISSN 1432-2250, doi:10.1007/s00162-018-0465 J. URL https://doi.org/10.1007/s00162-018-0465-1.